

We are IntechOpen, the world's leading publisher of Open Access books Built by scientists, for scientists

6,900

Open access books available

186,000

International authors and editors

200M

Downloads

Our authors are among the

154

Countries delivered to

TOP 1%

most cited scientists

12.2%

Contributors from top 500 universities



WEB OF SCIENCE™

Selection of our books indexed in the Book Citation Index
in Web of Science™ Core Collection (BKCI)

Interested in publishing with us?
Contact book.department@intechopen.com

Numbers displayed above are based on latest data collected.
For more information visit www.intechopen.com



Incoherent Scatter Radar — Spectral Signal Model and Ionospheric Applications

Erhan Kudeki¹ and Marco Milla²

¹University of Illinois at Urbana-Champaign

²Jicamarca Radio Observatory, Lima
Peru

1. Introduction

Doppler radars find a widespread use in the estimation of the velocity of discrete *hard-targets* as described elsewhere in this volume. In case of *soft-targets* — collections of vast numbers of weakly scattering elements filling the radar beam — the emphasis typically shifts to collecting the *statistics* of random motions of the scattering elements — i.e., Doppler spectral estimation — from which thermal or turbulent state of the target can be inferred, as appropriate. For instance, in case of a plasma in thermal equilibrium, e.g., the quiescent *ionosphere*, a Doppler radar of sufficient power-aperture-product can detect, in addition to the plasma drift velocities, the densities, temperatures, and even current densities of charged particle populations of the probed plasma — such Doppler radars used in ionospheric research are known as *incoherent scatter radars* (ISR). In this chapter we will provide a simplified description of ISR spectral theories (e.g., Kudeki & Milla, 2011) and also discuss magnetoionic propagation effects pertinent to ionospheric applications of ISR's at low latitudes. A second chapter in this volume focusing on in-beam imaging of soft-targets by Hysell & Chau (2012) is pertinent to non-equilibrium plasmas and complements the topics covered in this article.

The chapter is organized as follows: The working principles of ISR's and the general theory of incoherent scatter spectrum are described in Sections 2 and 3. ISR spectral features in unmagnetized and magnetized plasmas are examined in Sections 4 and 5, respectively. Coulomb collision process operating in magnetized ionosphere is described in Section 6. Effects of Coulomb collisions on particle trajectories and ISR spectra are discussed in Sections 7 and 8. Finally, Section 9 discusses the magnetoionic propagation effects on incoherent scattered radar signals. The chapter ends with a brief summary in Section 10.

2. Working principles of ISR's

The basic physical mechanism underlying the operation of ISR's is *Thomson scattering* of electromagnetic waves by ionospheric free electrons. Thomson scattering refers to the fact that free electrons brought into oscillatory motions by incident radar pulses will re-radiate like Hertzian dipoles at the frequency of the incident field. The total power of scattered fields in an ISR experiment is a resultant of interference effects between re-radiated field components arriving from free electrons occupying the radar field of view. Furthermore the frequency spectrum of incoherent scatter signal is shaped by the same interference effects in addition

to the distribution of random velocities of the electrons in the radar frame of reference in accordance with a two-way Doppler effect.

The “incoherent scatter” concept refers, in essence, to a scattering scenario where each of the Thomson scattering electrons would have statistically independent random motions. The total scattered power would then be reduced to a simple sum (see below) of the return power of individual electrons in the radar field of view treated as hard targets in terms of a standard radar equation, i.e.,

$$P_r = \frac{P_t G_t A_r}{(4\pi r^2)^2} \sigma_e, \quad (1)$$

with transmitted power and gain P_t and G_t , respectively, effective area A_r of the receiving antenna, radar range r , and backscatter radar-cross-section (RCS) of an individual electron, $\sigma_e \equiv 4\pi r_e^2$, where $r_e = e^2(4\pi\epsilon_0 mc^2)^{-1} \approx 2.181 \times 10^{-15}$ m is the classical electron radius.

Ionospheric electron motions are not fully independent — i.e., particle trajectories are partially correlated — however, and, as a consequence, the scattered radar power from the ionosphere deviates from such a simple sum in a manner that depends on several factors including the radar frequency, electron and ion temperatures, as well as ambient magnetic field of the ionospheric plasma. This deviation is just one of many manifestations of the correlations — also known as “collective effects” — between ionospheric charge carriers, including the deviation of the Doppler frequency spectrum of the scattered fields from a simple Gaussian shape (of thermal velocity distribution of electrons) implied by the ideal incoherent scatter scenario. It turns out that the “complications” introduced by the collective effects in the Doppler spectrum of this “not-exactly-incoherent-scatter” from the ionosphere amount to a wealth of information that can be extracted from the ISR spectrum given its proper forward model. This model will be described in the following sections.

Historical note: When ISR’s were first proposed (Gordon, 1958), it was expected that ionospheric scattering from free electrons would be fully incoherent. First ISR measurements (Bowles, 1958) showed that not to be the case. Realistic spectral models compatible with the measurements and correlated particle motions were developed subsequently. Rapid theoretical progress took place in the 1960’s, but issues related to ISR response at small magnetic aspect angles were resolved only very recently (e.g., Milla & Kudeki, 2011) as explained in Section 8.

3. From Thomson scatter to the general formulation of ISR spectrum

Since oscillating free electrons radiate like Hertzian dipoles, it can be shown, using elementary antenna theory, that the backscattered field amplitude¹ from an electron at a distance r to a radar antenna is (using phasor notation)

$$E_s = -\frac{r_e}{r} e^{-jk_0 r} E_i = -\frac{r_e}{r} E_0 e^{-j2k_0 r}, \quad (2)$$

where $E_i = E_0 e^{-jk_0 r}$ is the incident field phasor and $k_0 = \omega_0/c$ is the wavenumber of the incident wave with a carrier frequency ω_0 . It follows that a collection of scattering electrons

¹ Since transmitted and scattered fields are co-polarized we can avoid using a vector notation here.

filling a small radar volume ΔV will produce a scattered field²

$$E_s = - \sum_{p=1}^{N_o \Delta V} \frac{r_e}{r_p} E_{op} e^{-j2k_o r_p} \approx - \frac{r_e}{r} E_o \sum_{p=1}^{N_o \Delta V} e^{j\mathbf{k} \cdot \mathbf{r}_p}. \quad (3)$$

Here N_o is the mean density of free electrons within ΔV and the rightmost expression amounts to invoking a plane wave approximation³ of the incident and scattered fields in terms of scatterer position vector \mathbf{r}_p and a Bragg wave vector $\mathbf{k} = -2k_o \hat{r}$ pointing from the center of subvolume ΔV to the location of the radar antenna (assuming a mono-static backscatter radar geometry).

With electrons in (non-relativistic) motion, scattered field phasor (3) turns into

$$E_s(t) = - \frac{r_e}{r} E_o \sum_{p=1}^{N_o \Delta V} e^{j\mathbf{k} \cdot \mathbf{r}_p(t - \frac{r}{c})} \quad (4)$$

including a propagation time delay r/c of the scattered field from the center of volume⁴ ΔV . It then follows that the auto-correlation function (ACF) of the scattered field is

$$\langle E_s^*(t) E_s(t + \tau) \rangle = \frac{r_e^2}{r^2} |E_i|^2 \sum_{p=1}^{N_o \Delta V} \sum_{q=1}^{N_o \Delta V} \langle e^{j\mathbf{k} \cdot [\mathbf{r}_q(t + \tau - \frac{r}{c}) - \mathbf{r}_p(t - \frac{r}{c})]} \rangle, \quad (5)$$

where angular brackets denote an expected value (ensemble average) operation. Using $\langle e^{j\mathbf{k} \cdot [\mathbf{r}_q - \mathbf{r}_p]} \rangle = \langle e^{j\mathbf{k} \cdot \mathbf{r}_q} \rangle \langle e^{-j\mathbf{k} \cdot \mathbf{r}_p} \rangle = 0$ for statistically independent electrons ($p \neq q$), this reduces to

$$\langle E_s^*(t) E_s(t + \tau) \rangle = \frac{r_e^2}{r^2} |E_i|^2 N_o \Delta V \langle e^{j\mathbf{k} \cdot [\mathbf{r}_q(t + \tau - \frac{r}{c}) - \mathbf{r}_q(t - \frac{r}{c})]} \rangle = \frac{r_e^2}{r^2} |E_i|^2 N_o \Delta V \langle e^{j\mathbf{k} \cdot \Delta \mathbf{r}} \rangle \quad (6)$$

with $\Delta \mathbf{r} \equiv \mathbf{r}_q(t + \tau - \frac{r}{c}) - \mathbf{r}_q(t - \frac{r}{c})$ denoting particle displacements over time intervals τ . Only with (6), i.e., only under a strict incoherent scatter scenario, we can obtain

$$\langle |E_s(t)|^2 \rangle = \frac{r_e^2}{r^2} |E_i|^2 N_o \Delta V, \quad (7)$$

a result that implies a total scattered power which is a simple sum over all scatterers individually described by (1).

Collective effects in general invalidate the results (6) and (7) from being directly applicable. Nevertheless the desired spectral model for ionospheric incoherent scatter can be expressed in terms of (6) and (7) after suitable corrections and transformations. To obtain the model let us first re-express (4) as

$$E_s(t) = - \frac{r_e}{r} E_o n_e(\mathbf{k}, t - \frac{r}{c}) \quad (8)$$

² We assume here that ω_o is sufficiently large so that dispersion effects due to plasma density N_o can be neglected (or treated as perturbation effects). Also, multiple scattering is neglected.

³ Justified for $r > 2k_o \Delta V^{2/3} / \pi$, the far-field condition for an antenna of size $\Delta V^{1/3}$.

⁴ ΔV is sufficiently small for electrons to move only an insignificant fraction of the radar wavelength during an interval for light to propagate across ΔV .

in terms of 3D spatial Fourier transform

$$n_e(\mathbf{k}, t) \equiv \sum_{p=1}^{N_o \Delta V} e^{-j\mathbf{k} \cdot \mathbf{r}_p t} \quad (9)$$

of the *microscopic* density function $n_e(\mathbf{r}, t) = \sum_p \delta(\mathbf{r} - \mathbf{r}_p(t))$ of the electrons⁵ in volume ΔV . The scattered field spectrum for volume ΔV can then be expressed⁶ as

$$\langle |E_s(\omega)|^2 \rangle = \frac{r_e^2}{r^2} |E_i|^2 \langle |n_e(\mathbf{k}, \omega)|^2 \rangle \Delta V \quad (11)$$

in terms of the electron density frequency spectrum

$$\langle |n_e(\mathbf{k}, \omega)|^2 \rangle \equiv \int_{-\infty}^{\infty} d\tau e^{-j\omega\tau} \frac{1}{\Delta V} \langle n_e^*(\mathbf{k}, t - \frac{r}{c}) n_e(\mathbf{k}, t - \frac{r}{c} + \tau) \rangle \quad (12)$$

which simplifies as

$$\langle |n_e(\mathbf{k}, \omega)|^2 \rangle = N_o \int_{-\infty}^{\infty} d\tau e^{-j\omega\tau} \langle e^{j\mathbf{k} \cdot \Delta \mathbf{r}} \rangle \equiv \langle |n_{te}(\mathbf{k}, \omega)|^2 \rangle \quad (13)$$

for independent electrons. We also have an identical expression $\langle |n_{ti}(\mathbf{k}, \omega)|^2 \rangle$ describing the density spectrum independent ions in the same volume in terms of ion displacements $\Delta \mathbf{r}$.

While neither $\langle |n_{te}(\mathbf{k}, \omega)|^2 \rangle$ nor $\langle |n_{ti}(\mathbf{k}, \omega)|^2 \rangle$ are accurate representations of the density spectra of electrons and ions in a real ionosphere (because of the neglect of collective effects), it turns out that an accurate model for $\langle |n_e(\mathbf{k}, \omega)|^2 \rangle$ can be expressed as a linear combination of $\langle |n_{te}(\mathbf{k}, \omega)|^2 \rangle$ and $\langle |n_{ti}(\mathbf{k}, \omega)|^2 \rangle$ given by

$$\langle |n_e(\mathbf{k}, \omega)|^2 \rangle = \frac{|j\omega\epsilon_o + \sigma_i|^2 \langle |n_{te}(\mathbf{k}, \omega)|^2 \rangle}{|j\omega\epsilon_o + \sigma_e + \sigma_i|^2} + \frac{|\sigma_e|^2 \langle |n_{ti}(\mathbf{k}, \omega)|^2 \rangle}{|j\omega\epsilon_o + \sigma_e + \sigma_i|^2}, \quad (14)$$

where $\sigma_{e,i}$ denote the AC conductivities of electrons and ions in the medium. This result can be derived (e.g., Kudeki & Milla, 2011) by enforcing charge conservation (i.e., continuity equation) in a plasma carrying quasi-static *macroscopic* currents $\sigma_{e,i}E$ forced by longitudinal polarization fields⁷ E produced by the mismatch of thermally driven electron and ion density fluctuations $n_{te}(\mathbf{k}, t)$ and $n_{ti}(\mathbf{k}, t)$. Furthermore, Nyquist noise theorem (e.g., Callen & Welton, 1951) stipulates that the required conductivities are related to the thermal density spectra via relations

$$\frac{\omega^2}{k^2} e^2 \langle |n_{te,i}(\mathbf{k}, \omega)|^2 \rangle = 2KT_{e,i} \text{Re}\{\sigma_{e,i}(\mathbf{k}, \omega)\}. \quad (15)$$

⁵ Here $\delta(\cdot)$'s denote Dirac's deltas utilized to highlight the trajectories $\mathbf{r}_p(t)$ of individual electrons.

⁶ This expression can be generalized as a soft-target radar equation

$$P_r = \int \int \frac{|E_i|^2 / 2\eta_o}{4\pi r^2} A_r 4\pi r_e^2 \langle |n_e(\mathbf{k}, \omega)|^2 \rangle \frac{d\omega}{2\pi} dV \quad (10)$$

for backscatter ISR's having a scattering volume defined by the beam pattern associated with the effective area function $A_r(\mathbf{r})$.

⁷ Note that it is the response of individual particles to the quasi-static E that produces the mutual correlations in their motions.

And since $\sigma_{e,i}(\mathbf{k}, \omega)$ can be uniquely obtained from $\text{Re}\{\sigma_{e,i}(\mathbf{k}, \omega)\}$ using Kramer-Kronig relations (e.g., Yeh & Liu, 1972), a full blown solution of the modeling problem can be formulated in terms of “single particle correlations” $\langle e^{j\mathbf{k}\cdot\Delta\mathbf{r}} \rangle$ underlying the thermal density spectra $\langle |n_{te}(\mathbf{k}, \omega)|^2 \rangle$ and $\langle |n_{ti}(\mathbf{k}, \omega)|^2 \rangle$.

This general formulation is as follows (see Appendix 2 in Kudeki & Milla, 2011, for a detailed derivation): In terms of a one-sided integral transformation

$$J_s(\omega) \equiv \int_0^\infty d\tau e^{-j\omega\tau} \langle e^{j\mathbf{k}\cdot\Delta\mathbf{r}_s} \rangle, \quad (16)$$

known as *Gordeyev integral* for species s (e or i for the single-ion case), we have

$$\frac{\langle |n_{ts}(\mathbf{k}, \omega)|^2 \rangle}{N_0} = 2\text{Re}\{J_s(\omega_s)\} \quad \text{and} \quad \frac{\sigma_s(\mathbf{k}, \omega)}{j\omega\epsilon_0} = \frac{1 - j\omega_s J_s(\omega_s)}{k^2 h_s^2}, \quad (17)$$

where $\omega_s \equiv \omega - \mathbf{k} \cdot \mathbf{V}_s$ is a Doppler-shifted frequency in the radar frame due to mean velocity \mathbf{V}_s of species s , $h_s \equiv \sqrt{\epsilon_0 K T_s / N_0 e^2}$ is the corresponding Debye length, and the \mathbf{k} - ω spectrum of electron density fluctuations in the equilibrium plasma is given by (14) or its multi-ion generalizations.

The “general framework” of ISR spectral models represented by (16)-(17) and (14) (as well as (10)) takes care of the macrophysics of the incoherent scatter process due to collective effects, while microphysics details of the process remain to be addressed in the specification of single particle ACF's $\langle e^{j\mathbf{k}\cdot\Delta\mathbf{r}} \rangle$.

4. Single particle ACF's $\langle e^{j\mathbf{k}\cdot\Delta\mathbf{r}} \rangle$ for un-magnetized plasmas

We have just seen that ISR spectrum of ionospheric plasmas in thermal equilibrium can be specified in terms of single particle ACF's $\langle e^{j\mathbf{k}\cdot\Delta\mathbf{r}} \rangle$. In general, an ACF $\langle e^{j\mathbf{k}\cdot\Delta\mathbf{r}} \rangle$ can be explicitly computed if the probability distribution function (pdf) $f(\Delta r)$, where Δr is the component of $\Delta\mathbf{r}$ along \mathbf{k} , is known. Alternatively, $\langle e^{j\mathbf{k}\cdot\Delta\mathbf{r}} \rangle$ can also be computed directly given an ensemble of realizations of Δr for a given time delay τ . In either case, pdf's $f(\Delta r)$ or pertinent sets of Δr data will reflect the dynamics of random particle motions taking place in ionospheric plasmas.

When Δr is a Gaussian random variable with a pdf

$$f(\Delta r) = \frac{e^{-\frac{\Delta r^2}{2\langle\Delta r^2\rangle}}}{\sqrt{2\pi\langle\Delta r^2\rangle}}, \quad (18)$$

the single-particle ACF

$$\langle e^{j\mathbf{k}\cdot\Delta\mathbf{r}} \rangle = \int e^{jk\Delta r} f(\Delta r) d(\Delta r) = e^{-\frac{1}{2}k^2\langle\Delta r^2\rangle} \quad (19)$$

depends on the mean-square displacement $\langle\Delta r^2\rangle$ of the particles. In such cases incoherent scatter modeling problem reduces to finding the appropriate variance expressions $\langle\Delta r^2\rangle$.

In a non-magnetized and collisionless plasma the charge carriers will move along straight line (unperturbed) trajectories with random velocities \mathbf{v} . In that case the displacement vectors will be

$$\Delta\mathbf{r} = \mathbf{v}\tau \quad (20)$$

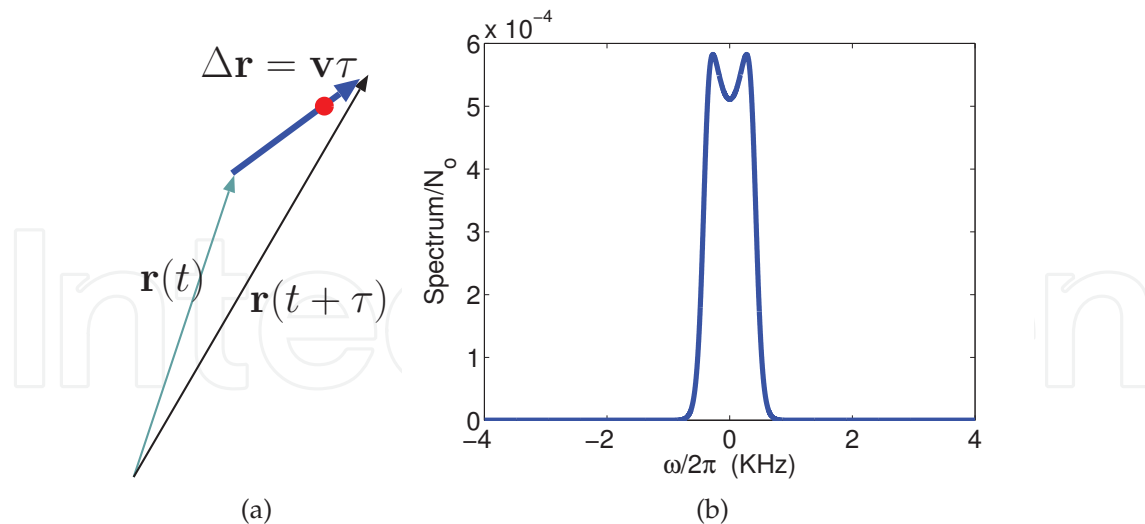


Fig. 1. (a) A cartoon depicting particle displacements Δr in a plasma with straight line charge carrier trajectories, and (b) a sample ISR spectrum for a non-magnetized and collisionless plasma in thermal equilibrium.

over intervals τ . Assuming Maxwellian distributed velocity components v along wavevector \mathbf{k} , we then have Gaussian distributed displacements $\Delta r = v\tau$ with variances

$$\langle \Delta r^2 \rangle = \langle v^2 \rangle \tau^2 = C^2 \tau^2, \quad (21)$$

where $C = \sqrt{KT/m}$ is the thermal speed of the charge carrier. The corresponding single particle ACF is in that case

$$\langle e^{j\mathbf{k} \cdot \Delta \mathbf{r}} \rangle = e^{-\frac{1}{2}k^2 C^2 \tau^2}, \quad (22)$$

which leads (via the general framework equations) to the most basic incoherent scatter spectral model exhibiting double humped shapes as depicted in Figure 6b when (22) is applied to both electrons and ions (with $C = C_e$ and C_i , respectively).

The ACF (22) is also applicable in collisional plasmas so long as the relevant “collision frequency” ν is small compared to the product kC , i.e., $\nu \ll kC$, so that an average particle moves a distance of many wavelengths $\frac{2\pi}{k}$ in between successive collisions. Otherwise, (22) will only be valid until the “first collisions” take place at $\tau \sim \nu^{-1}$. At larger τ , the mean-square displacement $\langle \Delta r^2 \rangle$ as well as the pdf $f(\Delta r)$ will in general depend on the details of the dominant collision process.

Long range Coulomb collisions between charged particles (e.g., electrons and ions) are frequently modeled as a “Brownian motion” process⁸, a procedure which leads (e.g., Kudeki & Milla, 2011) to a Gaussian $f(\Delta r)$ with a variance

$$\langle \Delta r^2 \rangle = \frac{2C^2}{\nu^2} (\nu\tau - 1 + e^{-\nu\tau}). \quad (23)$$

⁸ As discussed in Kudeki & Milla (2011) and here in Section 7, in Brownian motion the position and velocity increments are Gaussian random variables and correspond to stochastic solutions of a first-order Langevin update equation with constant coefficients.

The corresponding single particle ACF is

$$\langle e^{j\mathbf{k}\cdot\Delta\mathbf{r}} \rangle = e^{-\frac{k^2 C^2}{v^2}(\nu\tau - 1 + e^{-\nu\tau})}, \quad (24)$$

having the asymptotic limits (22) as well as

$$\langle e^{j\mathbf{k}\cdot\Delta\mathbf{r}} \rangle = e^{-\frac{k^2 C^2}{v} \tau} \quad (25)$$

for $\nu \ll kC$ and $\nu \gg kC$, respectively. Note that when (25) is applicable, with $\nu \gg kC$, an average particle moves across only a small fraction of a wavelength $\frac{2\pi}{k}$ in between successive collisions. In Coulomb interactions, the time ν^{-1} between “effective collisions” (an accumulated effect of interactions with many collision partners via their microscopic Coulomb fields) can be interpreted as the time interval over which the particle velocity vector rotates by about 90° .

Binary collisions of charge carriers with neutral atoms and molecules — dominant in the lower ionosphere — can be modeled as a Poisson process (Milla & Kudeki, 2009) and treated kinetically using the BGK collision operator (e.g., Dougherty & Farley, 1963). As shown in Milla & Kudeki (2009), in binary collisions with neutrals the mean-squared displacement of charge carriers is still given by (23), but the relevant pdf $f(\Delta r)$ is a Gaussian only for short and long delays τ satisfying $\nu\tau \ll 1$ and $\nu\tau \gg 1$, respectively. At intermediate τ 's the ACF of a collisional plasma dominated by binary collisions will then deviate from (24) and as a result collisional spectra will in general exhibit minor differences between binary and Coulomb collisions except in $\nu \ll kC$ and $\nu \gg kC$ limits (Hagfors & Brockelman, 1971; Milla & Kudeki, 2009).

As the above discussion implies, the single particle ACF in the high collision limit ($\nu \gg kC$) is insensitive to the distinctions between Coulomb and binary collisions and obeys a simple relation (25). In that limit it is fairly straightforward to evaluate the corresponding Gordeyev integrals analytically, and obtain (via the general framework equations) a Lorentzian shaped electron density spectrum (mainly the “ion-line”),

$$\frac{\langle |n_e(\mathbf{k}, \omega)|^2 \rangle}{N_o} \approx \frac{2k^2 D_i}{\omega^2 + (2k^2 D_i)^2}, \quad (26)$$

valid for $kh \ll 1$ (wavelength larger than Debye length), where $D_i \equiv C_i^2/\nu_i = KT_i/m_i\nu_i$ denotes the ion diffusion coefficient in the collisional plasma. This result is pertinent to D-region incoherent scatter observations (see Figure 2) neglecting possible complications due to the presence of negative ions (e.g., Mathews, 1984). Also, from (26) it follows that

$$\langle |n_e(\mathbf{k})|^2 \rangle \equiv \int_{-\infty}^{\infty} \frac{d\omega}{2\pi} \langle |n_e(\mathbf{k}, \omega)|^2 \rangle = \frac{N_o}{2}, \quad (27)$$

which is in fact true in general — i.e., for all types of plasmas with or without collisions and/or DC magnetic field — so long as $T_e = T_i$ and $kh \ll 1$. In view of radar equation (10), this result leads to a well-known volumetric radar cross-section (RCS) formula

$$4\pi r_e^2 \langle |n_e(\mathbf{k})|^2 \rangle = 2\pi r_e^2 N_o \quad (28)$$

for ISR's that is valid under the same conditions as (27). Hence, RCS measurements with ISR's can provide us with ionospheric mean densities N_o .

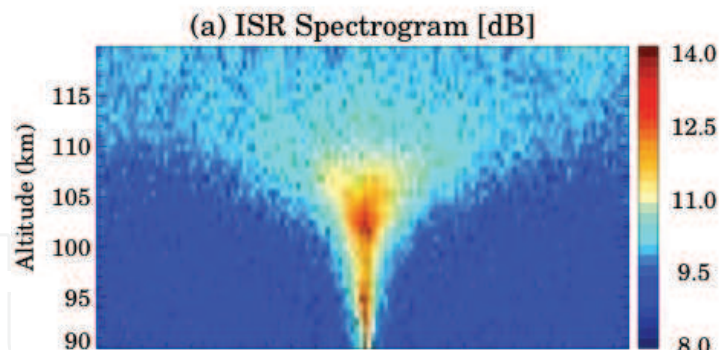


Fig. 2. Collisional D-region spectrograms from Jicamarca Radio Observatory (from Chau & Kudeki, 2006).

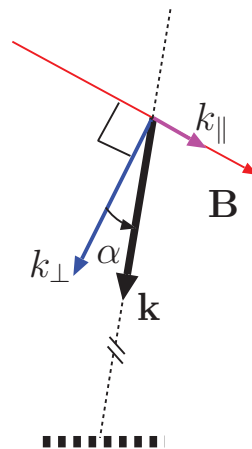


Fig. 3. Backscattering geometry in a magnetized ionosphere parametrized by wavevector components k_{\parallel} and k_{\perp} and aspect angle $\alpha = \tan^{-1}(k_{\parallel}/k_{\perp})$.

5. Incoherent scatter from a magnetized ionosphere

In a magnetized ionosphere with an ambient magnetic field \mathbf{B} , it is convenient to express the scattered wavevector as $\mathbf{k} = \hat{b}k_{\parallel} + \hat{p}k_{\perp}$, where \hat{b} and \hat{p} are orthogonal unit vectors on \mathbf{k} - \mathbf{B} plane which are parallel and perpendicular to \mathbf{B} , respectively, as depicted in Figure 3. We can then express the single particle ACF as

$$\langle e^{j\mathbf{k}\cdot\Delta\mathbf{r}} \rangle = \langle e^{j(k_{\parallel}\Delta r + k_{\perp}\Delta p)} \rangle = \langle e^{jk_{\parallel}\Delta r} \times e^{jk_{\perp}\Delta p} \rangle, \quad (29)$$

where Δr and Δp are particle displacements along unit vectors \hat{b} and \hat{p} . Assuming independent Gaussian random variables Δr and Δp , we can then write

$$\langle e^{j\mathbf{k}\cdot\Delta\mathbf{r}} \rangle = e^{-\frac{1}{2}k_{\parallel}^2\langle\Delta r^2\rangle} \times e^{-\frac{1}{2}k_{\perp}^2\langle\Delta p^2\rangle} \quad (30)$$

in analogy with the non-magnetized case. The assumptions are clearly justified in case of a collisionless ionosphere (or for intervals τ such that $\tau\nu \ll 1$), in which case

$$\langle\Delta r^2\rangle = C^2\tau^2 \quad (31)$$

and, as shown in Kudeki & Milla (2011),

$$\langle\Delta p^2\rangle = \frac{4C^2}{\Omega^2}\sin^2(\Omega\tau/2), \quad (32)$$

where $\Omega \equiv \frac{qB}{m}$ is the particle gyrofrequency. The mean-square displacement (32) which is periodic in τ is can be derived by invoking circular particle orbits with periods $2\pi/\Omega$ and mean radii $\sqrt{2}C/\Omega$ on the plane perpendicular to \mathbf{B} . As a consequence of (31) and (32), ISR spectra in a magnetized but collisionless ionosphere can be derived from the single particle ACF

$$\langle e^{j\mathbf{k}\cdot\Delta\mathbf{r}} \rangle = e^{-\frac{1}{2}k_{\parallel}^2 C^2 \tau^2} \times e^{-\frac{2k_{\perp}^2 C^2}{\Omega^2} \sin^2(\Omega\tau/2)} \quad (33)$$

for electrons and ions.

Note that the ACF (33) becomes periodic and the associated Gordeyev integrals and spectra become singular (expressed in terms of Dirac's deltas) in $k_{\parallel} \rightarrow 0$ limit. Spectral singularities are of course not observed in practice since collisions in a real ionosphere end up limiting the width of single particle ACF's in τ in the limit of small "aspect angles" $\alpha = \tan^{-1}(k_{\parallel}/k_{\perp})$.

Despite the singularities in (33), it turns out that for finite aspect angles α larger than a few degrees, the collisionless result (33) leads us to the most frequently used ISR spectral model at F-region heights. This is true because given a finite k_{\parallel} , the term $e^{-\frac{1}{2}k_{\parallel}^2 C^2 \tau^2}$ in (33) restricts the width of the ACF to a finite value of $\sim (k_{\parallel}C)^{-1}$ even in the absence of collisions (or when collision frequencies are smaller than $k_{\parallel}C$). It can then be shown that for $\tau \ll (k_{\parallel}C)^{-1}$, as well as $\Omega\tau \ll 2\pi$ (easily satisfied by massive ions), the ACF (33) for ions recombines to a simplified form $e^{-\frac{1}{2}k^2 C^2 \tau^2}$ as if the plasma were non-magnetized. Also with finite k_{\parallel} , the ACF (33) for electrons simplifies to $e^{-\frac{1}{2}k^2 \sin^2 \alpha C^2 \tau^2}$, since for the light electrons a condition $k_{\perp}C \ll \Omega$ can be easily invoked to ignore the rightmost exponential in (33) (or even more accurately, replace it with its average value over τ , namely, $1 - \frac{k_{\perp}^2 C^2}{\Omega^2}$). These ion and electron ACF's exhibit similar τ dependencies and lead to similar shaped Gordeyev integrals. The resulting ISR spectra are of the "double humped" type shown in Figure 1b.

6. Modeling the Coulomb collision effects in magnetized plasmas

As we have noted, the form (33) of the single particle ACF indicates that magnetic field effects in ISR response are confined to small aspect angles, which is also the regime where collision effects cannot be neglected (e.g., Farley, 1964; Sulzer & González, 1999; Woodman, 1967) given the non-physical behavior of ACF (33) in $\alpha \rightarrow 0^\circ$ limit.

Historical note: The need to account for the effects of collisions in incoherent scatter theory of ionospheric F-region returns was first pointed out by Farley (1964). Based on a qualitative analysis, Farley recognized that ion Coulomb collisions would be responsible for the lack of O^+ gyroresonance signatures on incoherent scatter observations carried out at 50 MHz at the Jicamarca Radio Observatory located near Lima, Peru. This analysis was later verified by the theoretical work of Woodman (1967) which was based on the simplified Fokker-Planck collision model of Dougherty (1964). Many years later, after the application of modern radar and signal processing techniques to the measurement and analysis of ISR signals (e.g., Kudrinskiy et al., 1999), Sulzer & González (1999) noted that, in addition to ion collisions, electron Coulomb collisions also have an influence on the shape of the ISR spectra at small magnetic aspect angles. Based on a more complex Fokker-Planck Coulomb collision model, Sulzer & González found that the collisional spectrum is narrower (just like the observations of Kudrinskiy et al., 1999) than what the collisionless theory predicts and that the effect of electron collisions extends up to relatively large magnetic aspect angles. Recently, this work has been refined and

extended by Milla & Kudeki (2011). The new procedure allows the calculation of collisional IS spectra at all magnetic aspect angles including the perpendicular-to- \mathbf{B} direction ($\alpha = 0^\circ$) as needed for IS radar applications. In this section, we present the procedure developed by Milla & Kudeki (2011) to model the effects of Coulomb collisions on the incoherent scatter spectrum.

The single-particle ACF $\langle e^{j\mathbf{k}\cdot\Delta\mathbf{r}} \rangle$ in a collisional plasma including a magnetic field can in principle be calculated by taking the spatial Fourier transform of the probability distribution $f(\Delta\mathbf{r}, \tau)$ of the particle displacement $\Delta\mathbf{r}$ appropriate for such plasmas, and $f(\Delta\mathbf{r}, \tau)$ in turn can be derived from the solution $f(\mathbf{r}, t)$ of the Boltzmann kinetic equation with a collision operator, e.g., the Fokker-Planck kinetic equation of Rosenbluth et al. (1957). Although, analytical solutions of simplified versions of the Fokker-Planck kinetic equation are available (e.g., Chandrasekhar, 1943; Dougherty, 1964), determining $f(\Delta\mathbf{r}, \tau)$ would be a daunting task when the full Fokker-Planck equation is considered.

We will discuss here an alternative and more practicable approach that involves Monte Carlo simulations of sample paths $\mathbf{r}(t)$ of particles undergoing Coulomb collisions. A sufficiently large set of samples of trajectories $\mathbf{r}(t)$ can then be used to compute $\langle e^{j\mathbf{k}\cdot\Delta\mathbf{r}} \rangle$ as well as any other statistical function of $\Delta\mathbf{r}$ assuming the random process $\mathbf{r}(t)$ to be ergodic. This alternate procedure requires the availability of a stochastic equation describing how the particle velocities

$$\mathbf{v}(t) \equiv \frac{d\mathbf{r}}{dt} \quad (34)$$

may evolve under the influence of Coulomb collisions.

Assuming that under Coulomb collisions the velocities $\mathbf{v}(t)$ constitute a Markovian random process — meaning that past values of \mathbf{v} would be of no help in predicting its future values if the present value is available — the stochastic evolution equation of $\mathbf{v}(t)$ will be constrained by very strict self-consistency conditions discussed by Gillespie (1996a;b) to acquire the form of a Langevin equation

$$\frac{d\mathbf{v}(t)}{dt} = \mathbf{A}(\mathbf{v}, t) + \bar{\mathbf{C}}(\mathbf{v}, t)\mathbf{W}(t) \quad (35)$$

where vector $\mathbf{A}(\mathbf{v}, t)$ and matrix $\bar{\mathbf{C}}(\mathbf{v}, t)$ consist of arbitrary smooth functions of arguments \mathbf{v} and t , and $\mathbf{W}(t)$ is a random vector having statistically independent Gaussian white noise components

$$W_i(t) = \lim_{\Delta t \rightarrow 0} \mathcal{N}(0, 1/\Delta t), \quad (36)$$

compatible with the requirement that $\langle W_i(t + \tau)W_i(t) \rangle = \delta(\tau)$. Here and elsewhere $\mathcal{N}(\mu, \sigma^2)$ denotes the normal random variable with mean μ and variance σ^2 .

A more natural way of expressing the Langevin equation (35) is to cast it in an update form, namely

$$\mathbf{v}(t + \Delta t) = \mathbf{v}(t) + \mathbf{A}(\mathbf{v}, t) \Delta t + \bar{\mathbf{C}}(\mathbf{v}, t) \Delta t^{1/2} \mathbf{U}(t), \quad (37)$$

where Δt is an infinitesimal update interval and $\mathbf{U}(t)$ is a vector composed of independent zero-mean Gaussian random variables with unity variance, i.e., $U_i(t) = \mathcal{N}(0, 1)$.

Note that the Langevin equation describing a Markovian process has the form of Newton's second law of motion, with the terms on the right representing forces per unit mass exerted on plasma particles. Considering the Lorentz force on a charged particle in a magnetized plasma with a constant magnetic field \mathbf{B} , and not violating the strict format of (35), we can modify the equation by adding a term $q\mathbf{v}(t) \times \mathbf{B}/m$ to its right hand side.

Another relevant fact is that a special type of Markov process characterized by a linear $\mathbf{A}(\mathbf{v}, t) = -\beta\mathbf{v}$ and a constant matrix $\bar{\mathbf{C}} = D^{1/2}\bar{\mathbf{I}}$, independent of \mathbf{v} and t , is known as Brownian motion process (e.g., Chandrasekhar, 1942; Uhlenbeck & Ornstein, 1930), which is often invoked in simplified models of collisional plasmas (e.g., Dougherty, 1964; Holod et al., 2005; Woodman, 1967) including our earlier result (24) with $\nu = \beta$. In these models, friction and diffusion coefficients, β and D , are constrained to be related by

$$D = \frac{2KT}{m}\beta \quad (38)$$

for a plasma in thermal equilibrium.

In return for having restricted $\mathbf{v}(t)$ to the space of Markovian processes, we have gained a stochastic evolution equation (35) with a plausible Newtonian interpretation and with the potential of taking us beyond Brownian motion based collision models. Furthermore, the evolution of probability density $f(\mathbf{v}, t)$ of a random variable $\mathbf{v}(t)$ is known to be governed, when $\mathbf{v}(t)$ is Markovian, by the Fokker-Planck kinetic equation having a “friction vector” and “diffusion tensor”

$$\left\langle \frac{\Delta\mathbf{v}}{\Delta t} \right\rangle_c = \mathbf{A}(\mathbf{v}, t), \quad (39)$$

and

$$\left\langle \frac{\Delta\mathbf{v}\Delta\mathbf{v}^T}{\Delta t} \right\rangle_c = \bar{\mathbf{C}}(\mathbf{v}, t)\bar{\mathbf{C}}^T(\mathbf{v}, t), \quad (40)$$

respectively, specified in terms of the input functions of the Langevin equation. This intimate link between the Langevin and Fokker-Planck equations — in describing Markovian processes from two different but mutually compatible perspectives — was first pointed out by Chandrasekhar (1943) and discussed in detail by Gillespie (1996b).

Since the Fokker-Planck friction vector and diffusion tensor for equilibrium plasmas with Coulomb interactions have already been worked out by Rosenbluth et al. (1957) as

$$\left\langle \frac{\Delta\mathbf{v}}{\Delta t} \right\rangle_c = -\beta(v)\mathbf{v} \quad (41)$$

and

$$\left\langle \frac{\Delta\mathbf{v}\Delta\mathbf{v}^T}{\Delta t} \right\rangle_c = \frac{D_{\perp}(v)}{2}\bar{\mathbf{I}} + \left(D_{\parallel}(v) - \frac{D_{\perp}(v)}{2} \right) \frac{\mathbf{v}\mathbf{v}^T}{v^2}, \quad (42)$$

in terms of scalar functions $\beta(v)$, $D_{\parallel}(v)$, $D_{\perp}(v)$, it follows that the Langevin update equation, magnetized version of (37), can be written as

$$\begin{aligned} \mathbf{v}(t + \Delta t) = & \mathbf{v}(t) + \frac{q}{m}\mathbf{v}(t) \times \mathbf{B} \Delta t \\ & - \beta(v)\Delta t \mathbf{v}(t) + \sqrt{D_{\parallel}(v)\Delta t} U_1 \hat{v}_{\parallel} + \sqrt{D_{\perp}(v)\frac{\Delta t}{2}} (U_2 \hat{v}_{\perp 1} + U_3 \hat{v}_{\perp 2}), \end{aligned} \quad (43)$$

where $\hat{v}_{\parallel}(t)$, $\hat{v}_{\perp 1}(t)$, and $\hat{v}_{\perp 2}(t)$ denote an orthogonal set of unit vectors parallel and perpendicular to the particle trajectory and $U_i(t) = \mathcal{N}(0, 1)$ are independent random numbers. For weakly magnetized plasmas of interest here, where Debye lengths are smaller than the mean gyro radii, the “friction coefficient” $\beta(v)$ and velocity-space diffusion

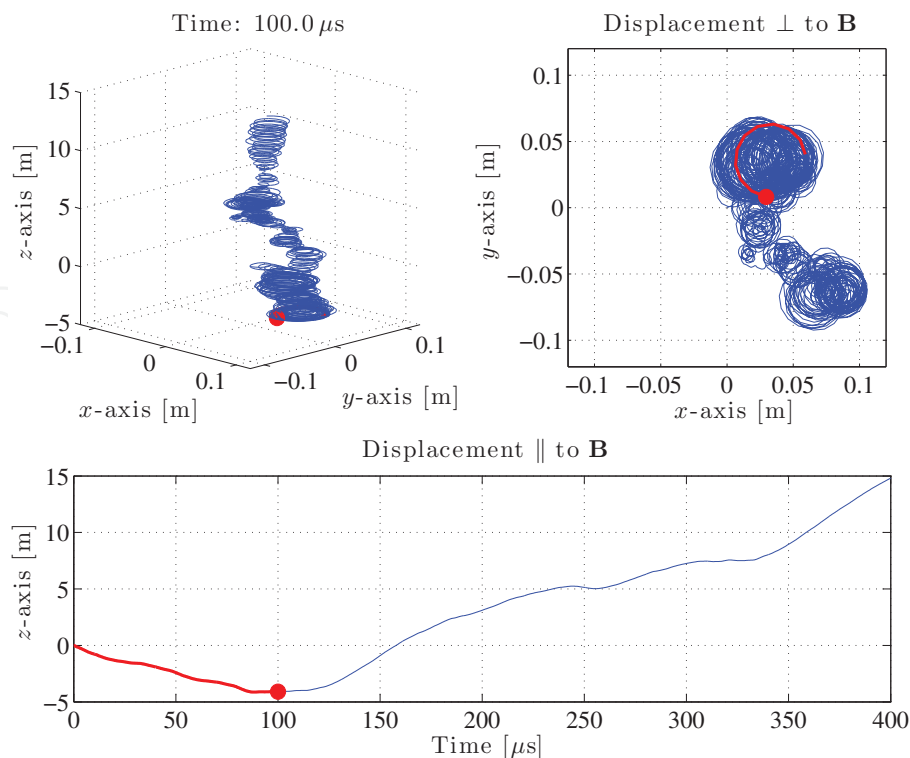


Fig. 4. Sample trajectory of an electron moving in an O⁺ plasma with density $N_e = 10^{12} \text{ m}^{-3}$, temperatures $T_e = T_i = 1000 \text{ K}$, and an ambient magnetic field $\mathbf{B} = \hat{z}25000 \text{ nT}$. Top left panel depicts the trajectory in 3D space; projection on the x - y plane (the plane perpendicular to \mathbf{B}) is shown on the right; displacements parallel to \mathbf{B} are depicted in the bottom plot (from Milla & Kudeki, 2011).

coefficients $D_{\parallel}(v)$ and $D_{\perp}(v)$ needed in (43) take the forms derived by Rosenbluth et al. (1957) which, for Maxwellian plasmas, have the Spitzer forms given in Milla & Kudeki (2011).

The velocity update equation (43) just described, along with its position counterpart

$$\mathbf{r}(t + \Delta t) = \mathbf{r}(t) + \mathbf{v}(t) \Delta t, \quad (44)$$

constitute our model equations for examining the effects of Coulomb collisions on incoherent scatter response from magnetized plasmas. These equations are used to simulate particle trajectories such as one shown in Figure 4 from which particle displacement statistics needed in ISR spectral models are estimated as explained in Sections 7 and 8.

7. Coulomb collision effects on ion and electron trajectories

7.1 Statistics of ion displacements

First we use the update equations (43) and (44) to simulate sample trajectories $\mathbf{r}(\mathbf{t})$ of an ion, e.g., an oxygen ion O⁺, moving in an ionospheric plasma with suppressed collective interactions but experiencing Coulomb collisions. Using the trajectory data, we can build up the probability distributions of the displacements $\Delta \mathbf{r}$ in directions perpendicular and parallel to the magnetic field for different time delays. Analyzing both distributions (parallel and perpendicular), we notice that their shapes are in essence Gaussian for time delays smaller than the inverse of the corresponding collision frequency. In Figure 5, we show examples

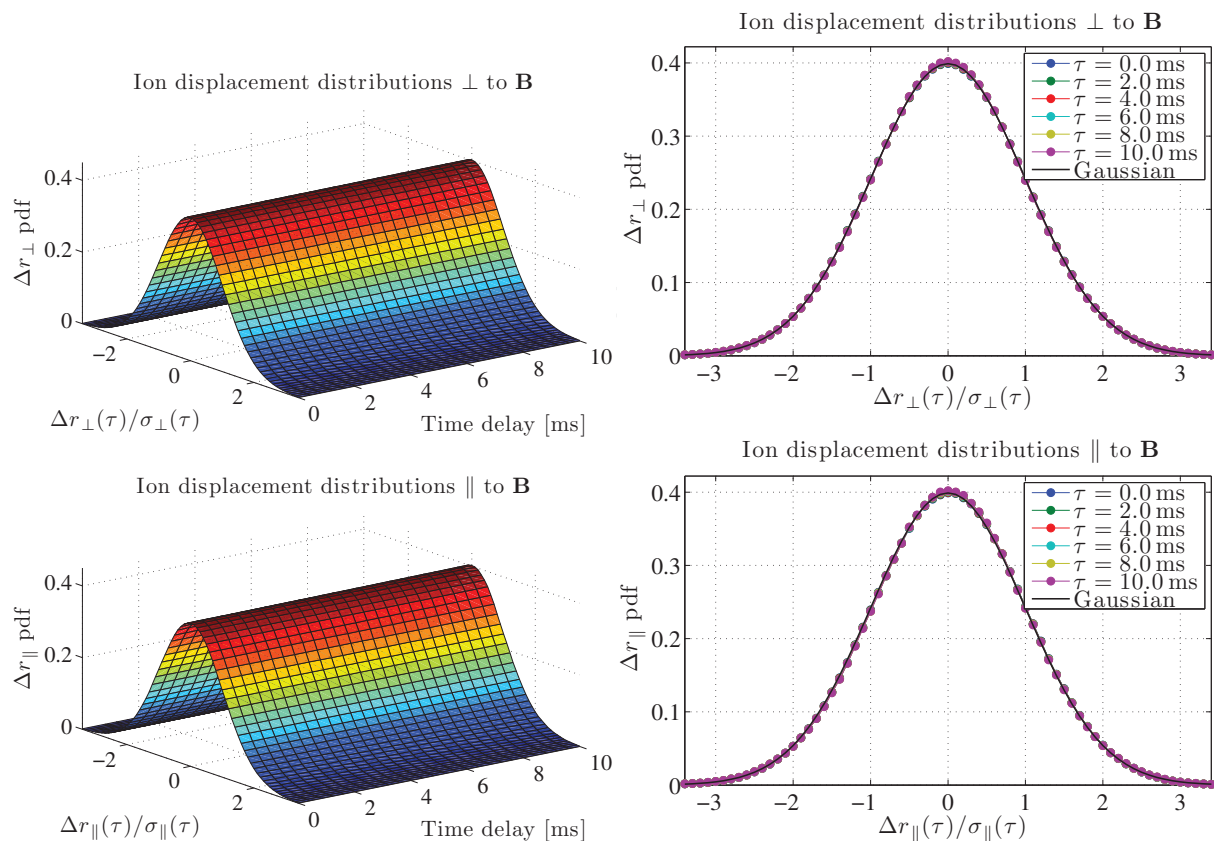


Fig. 5. Probability distributions of the displacements of a test ion in the directions perpendicular (top panels) and parallel (bottom panels) to the magnetic field. On the left, the displacement pdf's are displayed as functions of time delay τ . On the right, sample cuts of the pdf's are compared to a Gaussian distribution. Note that all distributions at all time delays are normalized to unit variance. The displacement axis of each distribution at every delay τ is scaled with the corresponding standard deviation of the simulated displacements (from Milla & Kudeki, 2011).

of the distributions of the ion displacements in the directions perpendicular and parallel to the magnetic field. In this case, we have considered an oxygen ion moving in a plasma with density $N_e = 10^{12} \text{ m}^{-3}$, temperatures $T_e = T_i = 1000 \text{ K}$ and magnetic field $B_0 = 25000 \text{ nT}$. Note that, at every delay τ , the distributions have been normalized to unit variance by scaling the displacement axis of each distribution with the corresponding standard deviation of the particle displacements. On the left panels, the distributions are displayed as functions of τ , while, on the right panels, sample cuts of these distributions are compared to a Gaussian pdf showing good agreement. In addition, we can verify that the components of the vector displacement (i.e., Δr_x , Δr_y , and Δr_z) are mutually uncorrelated.

This analysis implies that ion particle displacements can be represented as jointly Gaussian $\Delta \mathbf{r}$ components, therefore the single-particle ACF takes the form (e.g., Kudeki & Milla, 2011)

$$\langle e^{j\mathbf{k} \cdot \Delta \mathbf{r}} \rangle = e^{-\frac{1}{2}k^2 \sin^2 \alpha \langle \Delta r_{\parallel}^2 \rangle} \times e^{-\frac{1}{2}k^2 \cos^2 \alpha \langle \Delta r_{\perp}^2 \rangle}, \quad (45)$$

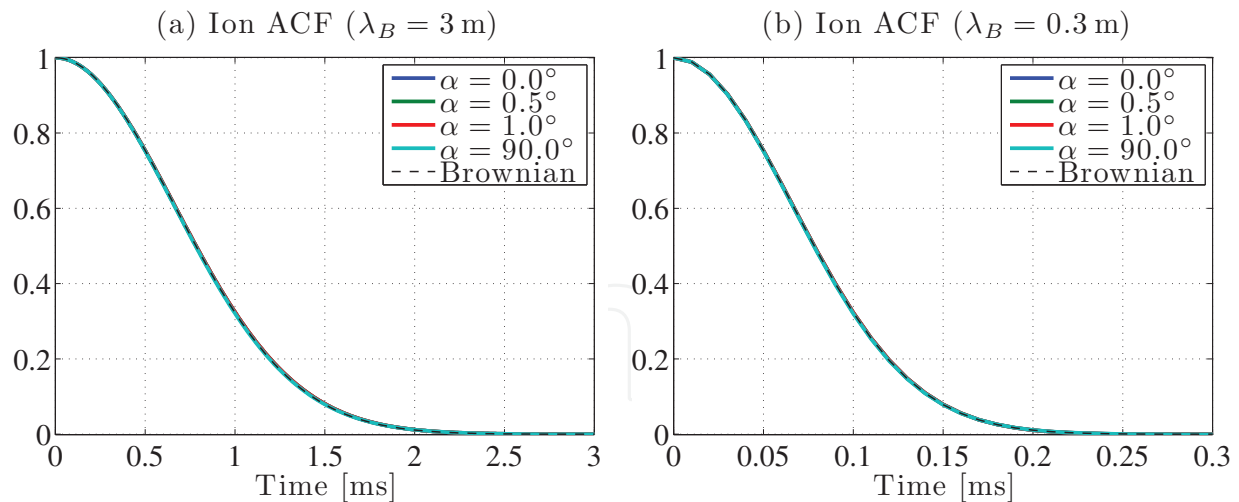


Fig. 6. Simulated single-ion ACF's at different magnetic aspect angles α for two radar Bragg wavelengths: (a) $\lambda_B = 3$ m and (b) $\lambda_B = 0.3$ m. The simulation results (color lines) are compared to theoretical ACF's computed using expression (51) of the Brownian-motion approximation (dashed lines). Note that there is effectively no dependence on aspect angle α (from Milla & Kudeki, 2011).

where, assuming a Brownian-motion process with distinct friction coefficients ν_{\parallel} and ν_{\perp} in the directions parallel and perpendicular to \mathbf{B} , the mean square displacements will vary as

$$\langle \Delta r_{\parallel}^2 \rangle = \frac{2C^2}{\nu_{\parallel}^2} (\nu_{\parallel} \tau - 1 + e^{-\nu_{\parallel} \tau}) \quad (46)$$

and

$$\langle \Delta r_{\perp}^2 \rangle = \frac{2C^2}{\nu_{\perp}^2 + \Omega^2} (\cos(2\gamma) + \nu_{\perp} \tau - e^{-\nu_{\perp} \tau} \cos(\Omega \tau - 2\gamma)) \quad (47)$$

in which $\gamma \equiv \tan^{-1}(\nu_{\perp}/\Omega)$, and $C \equiv \sqrt{KT/m}$ and $\Omega \equiv qB/m$ are, respectively, the thermal speed and gyrofrequency of the particles. Furthermore, simulated $\langle \Delta r_{\parallel, \perp}^2 \rangle$ match (46) and (47) with

$$\nu_{\perp} \approx \nu_{\parallel} \approx \nu_{i/i} \quad (48)$$

where

$$\nu_{i/i} = \frac{N_e e^4 \ln \Lambda_i}{12 \pi^{3/2} \epsilon_0^2 m_i^2 C_i^3} \quad (49)$$

is the Spitzer ion-ion collision frequency given by Callen (2006) and Milla & Kudeki (2011).

The simulations also indicate, in the case of oxygen ions,

$$\langle \Delta r_{\parallel}^2 \rangle \approx \langle \Delta r_{\perp}^2 \rangle \approx C_i^2 \tau^2 \quad (50)$$

for short time delays $\nu_{\parallel} \tau \ll 1$ and $\nu_{\perp} \tau < \Omega_i \tau \ll 1$, in consistency with (46) and (47). Hence (45) simplifies to

$$\langle e^{j\mathbf{k} \cdot \Delta \mathbf{r}_i} \rangle \approx e^{-\frac{1}{2} k^2 C_i^2 \tau^2}. \quad (51)$$

Evidently, the single-oxygen-ion ACF's are essentially the same as in collisionless and non-magnetized plasmas because (a) the ions move by many Bragg wavelengths $\lambda_B = 2\pi/k$

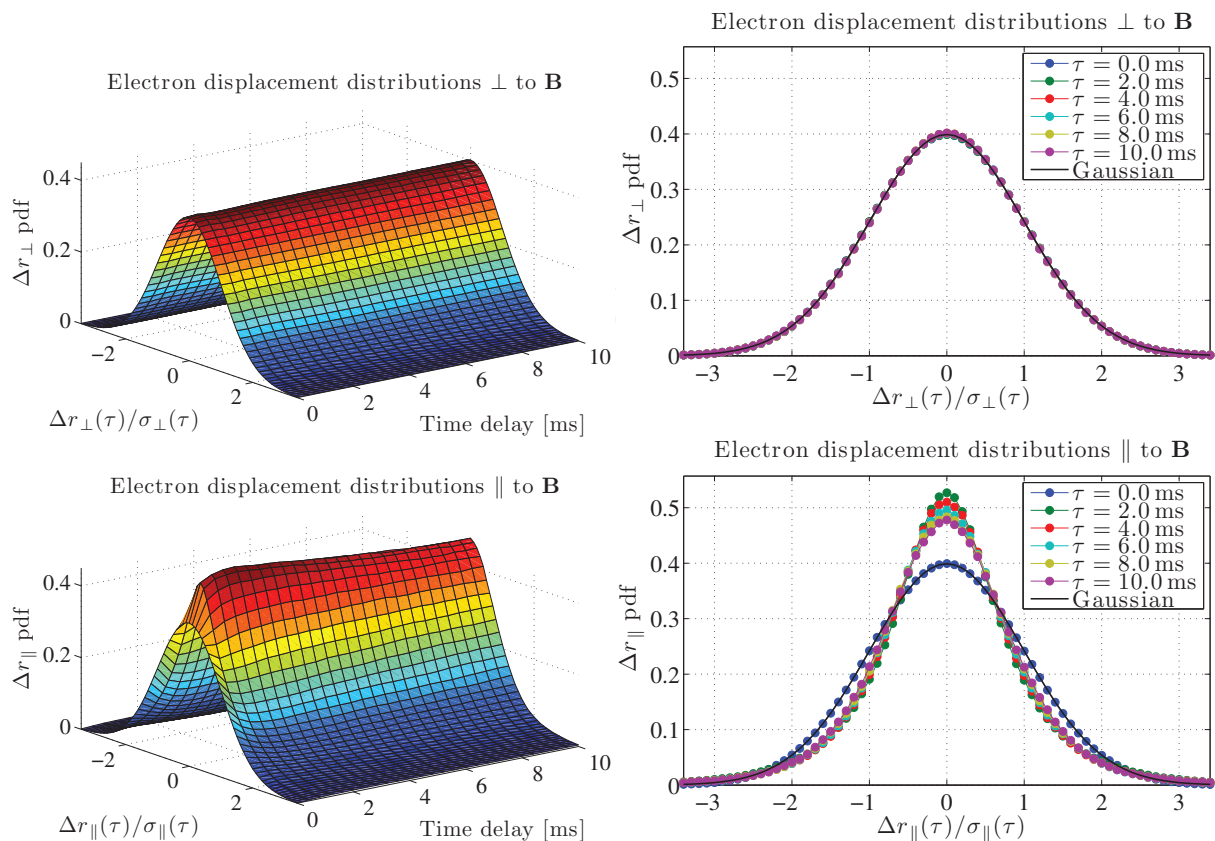


Fig. 7. Same as Figure 5 but for the case of a test electron. All distributions at all time delays are normalized to unit variance. Note that the distributions of the displacements parallel to \mathbf{B} become narrower than a Gaussian distribution (from Milla & Kudeki, 2011).

between successive Spitzer collisions, and (b) the ions are unable to return to within $\lambda_B/2\pi$ of their starting positions after a gyro-period as a consequence of Coulomb collisions. As an upshot, we will be able to handle the ion terms analytically in spectral calculations.

7.2 Statistics of electron displacements

Next, we study the effects of Coulomb collisions on electron trajectories using procedures similar to those applied to ions. In Figure 7, the displacement distributions resulting from an electron moving in an O+ plasma are presented. The top and bottom panels in Figure 7 correspond, respectively, to displacement distributions in perpendicular and parallel directions. On the left, the distributions are displayed as functions of τ , while on the right, sample cuts of the distributions are compared to a Gaussian pdf. As in the ion case, we note that the normalized distributions for perpendicular direction to be invariant with τ and closely match a Gaussian. However, the distributions of parallel displacements change with τ , and the shapes are distinctly non-Gaussian for intermediate values of τ . More specifically, at very small time delays (lower than the inverse of a collision frequency), the distributions are Gaussian, but then, in a few “collision” times, the distribution curves become more “spiky” (positive kurtosis) than a Gaussian. Although, at even longer delays τ the distributions once again relax to a Gaussian shape, it is clear that the electron displacement in the direction parallel to \mathbf{B} is not a Gaussian random variable at all time delays τ .

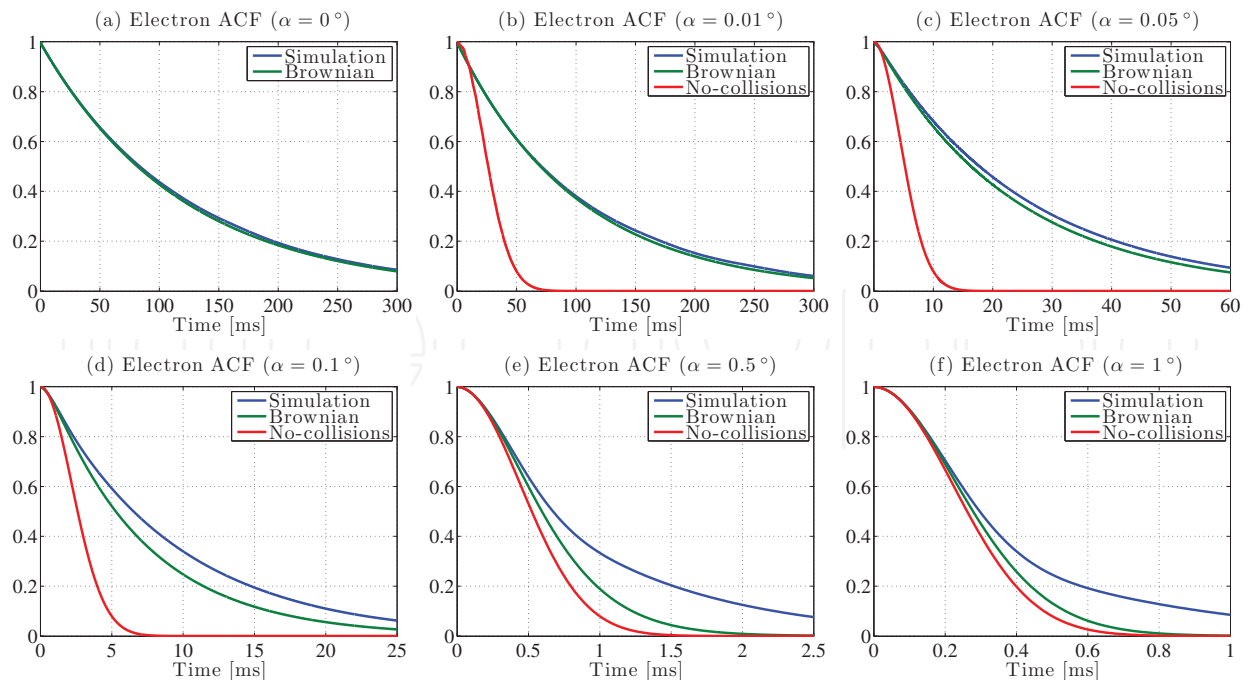


Fig. 8. Electron ACF's for $\lambda_B = 3$ m at different magnetic aspect angles: (a) $\alpha = 0^\circ$, (b) $\alpha = 0.01^\circ$, (c) $\alpha = 0.05^\circ$, (d) $\alpha = 0.1^\circ$, (e) $\alpha = 0.5^\circ$, and (f) $\alpha = 1^\circ$. Note the different time scales used in each plot (from Milla & Kudeki, 2011).

Fitting the simulated $\langle \Delta r_{\parallel, \perp}^2 \rangle$ to match (46) and (47) we find

$$v_{\parallel} \approx v_{e/i} \quad (52)$$

and

$$v_{\perp} \approx v_{e/i} + v_{e/e} \quad (53)$$

where

$$v_{e/e} = \frac{N_e e^4 \ln \Lambda_e}{12 \pi^{3/2} \epsilon_0^2 m_e^2 C_e^3} \quad (54)$$

and

$$v_{e/i} = \sqrt{2} v_{e/e} = \frac{\sqrt{2} N_e e^4 \ln \Lambda_e}{12 \pi^{3/2} \epsilon_0^2 m_e^2 C_e^3} \quad (55)$$

are the Spitzer electron-electron and electron-ion collision frequencies. However, the Brownian ACF model (45) fails to fit the electron ACF's $\langle e^{j\mathbf{k} \cdot \Delta \mathbf{r}_e} \rangle$ computed with simulated trajectories as shown in Figure 8 for a range of magnetic aspect angles and $\lambda_B = 3$ m. The blue curves correspond to the ACF's calculated with the Fokker-Planck model (simulations), while the green curves are the electron ACF's calculated using expression (45) together with our approximations for v_{\parallel} and v_{\perp} . Additionally, the electron ACF's for a collisionless magnetized plasma are also plotted (red curves). We can see that the Fokker-Planck and the Brownian ACF's matched almost perfectly at $\alpha = 0^\circ$, and also that the agreement is still good at very small magnetic aspect angles (see panels a, b, and c). However, substantial differences between the Brownian and estimated ACF's become evident as the magnetic aspect angle increases (see panels d, e, and f).

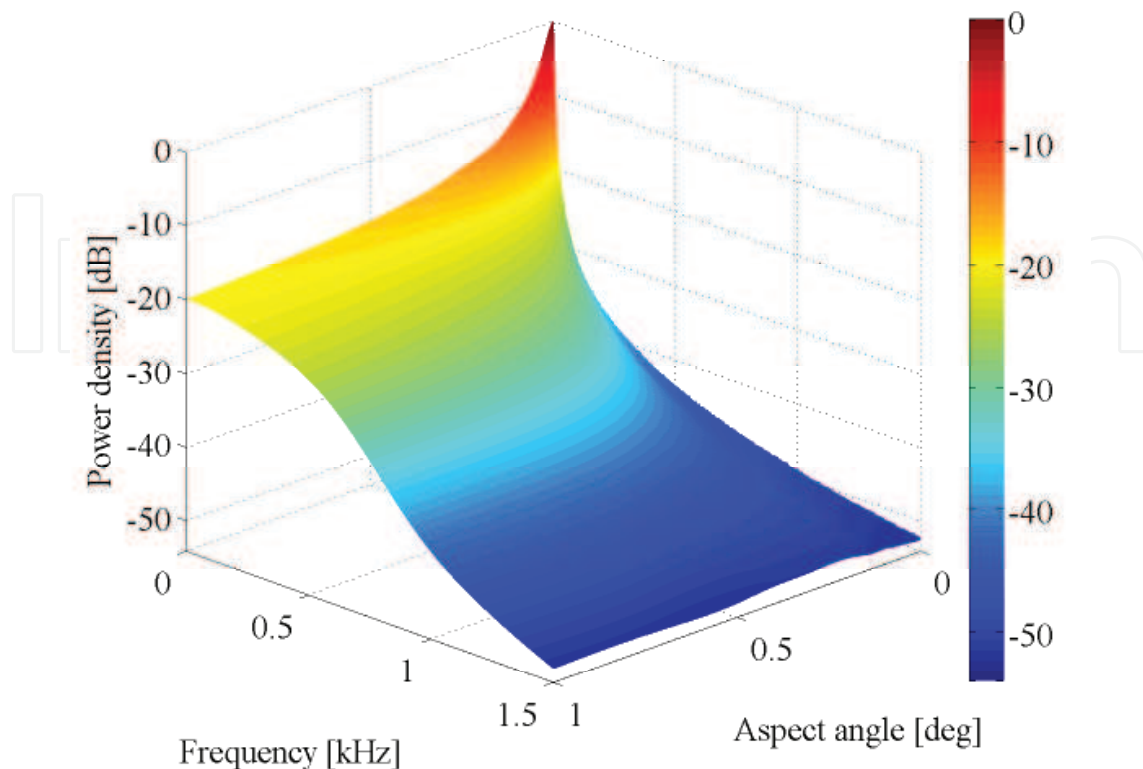


Fig. 9. Collisional incoherent scatter spectra as a function of magnetic aspect angle and Doppler frequency for $\lambda_B = 3$ m (e.g., Jicamarca radar Bragg wavelength). An O^+ plasma is considered (from Milla & Kudeki, 2011).

In summary, the single-electron ACF's needed for ISR spectral calculations cannot be obtained from Brownian motion model (45) at small aspect angles. This necessitates the construction of a numerical “library” compiled from Monte Carlo simulations based on the Langevin equation. The fundamental reason for this is the deviation of the electron displacements parallel to \mathbf{B} from Gaussian statistics, despite the fact that displacement variances are well modeled by the Brownian model. Certainly, a non-Gaussian process cannot be fully characterized by a model that specifies its first and second moments only; this is particularly true for the estimation of the characteristic function of the process $\langle e^{j\mathbf{k}\cdot\Delta\mathbf{r}_e} \rangle$ that depends on all the moments of the process distribution.

8. ISR spectrum for the magnetized ionosphere including Coulomb collision effects

The general framework of incoherent scatter theory formulates the spectrum in terms of the Gordoyev integrals or the corresponding single-particle ACFs for each plasma species. As discussed above, in the case of Coulomb collisions, the single-ion ACF can be approximated using the analytical expression (45). However, in the case of the electrons, the approximation of the electron motion as a Brownian process is not accurate, and thus, Monte Carlo calculations were needed to model single-electron ACFs and Gordeyev integrals for different sets of plasma parameters.

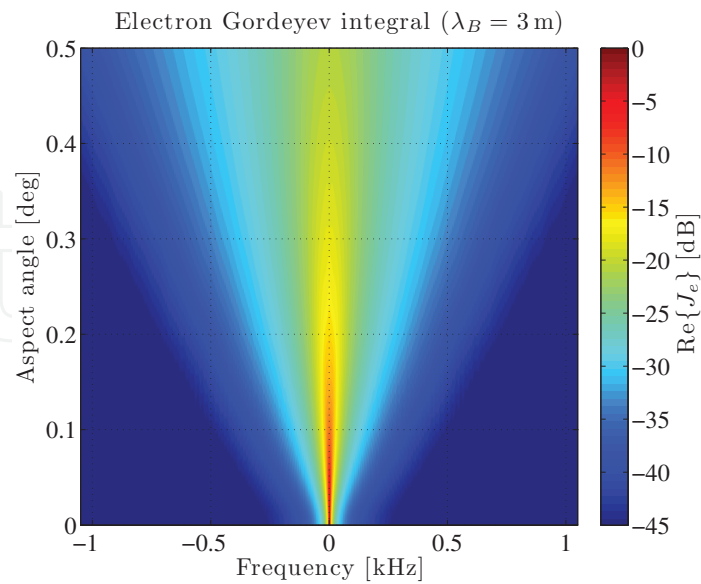


Fig. 10. Electron Gordeyev integral as functions of Doppler frequency and magnetic aspect angle for radar Bragg wavelength $\lambda_B = 3$ m. An O+ plasma with electron density $N_e = 10^{12} \text{ m}^{-3}$, temperatures $T_e = T_i = 1000$ K, and magnetic field $B_0 = 25$ T is considered (from Milla & Kudeki, 2011).

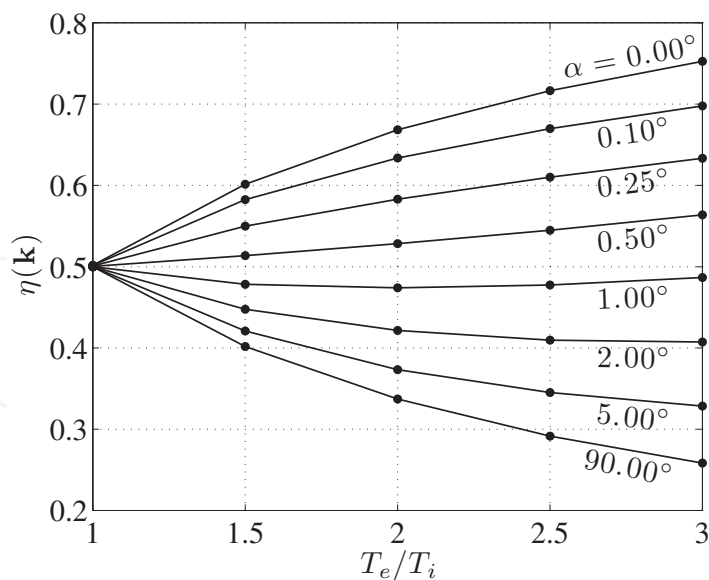


Fig. 11. Electron scattering efficiency factor $\eta(k)$ resulting from the frequency integration of the collisional incoherent scatter spectra as a function of electron-to-ion temperature ratio T_e/T_i and magnetic aspect angle α . An O+ plasma with $N_e = 10^{12} \text{ m}^{-3}$, $T_i = 1000$ K, and $B_0 = 25$ T is considered (from Milla & Kudeki, 2011).

Figure 9 shows a surface plot constructed from full IS spectrum calculations for $\lambda_B = 3$ m (e.g., for the 50 MHz Jicamarca ISR system located near Lima, Peru) using the ACF library constructed with the Monte Carlo procedure for electrons. The underlying electron Gordeyev integral $J_e(\omega)$ is presented in Figure 10 where only $\text{Re}\{J_e(\omega)\} \propto \langle |n_{te}(\mathbf{k}_B, \omega)|^2 \rangle$ is displayed. The plots are displayed as a functions of aspect angle α and Doppler frequency $\omega/2\pi$. In both figures it can be observed how these spectral functions sharpen significantly at small aspect angles. In particular in the case of the IS spectrum, we can see that, just in the range between 0.1° and 0° , the amplitude of the spectrum becomes ten times larger while its bandwidth is reduced by the same factor.

Some interesting features of the IS spectrum caused by collisions can be pointed out. As discussed by Milla & Kudeki (2011), in the absence of collisions, the magnetic field restricts the motion of electrons in the plane perpendicular to \mathbf{B} , forcing them to gyrate perpetually around the same magnetic field lines — this would generate infinite correlation time of the IS signal. With collisions, the electrons manage to diffuse *across* the field lines, and consequently the correlation time of the IS signal becomes finite. As a result, in the limit of $\alpha \rightarrow 0^\circ$, the width of the spectrum becomes proportional to the collision frequency. However, at other magnetic aspect angles, the effects are slightly different. In a few hundredths of a degree from perpendicular to \mathbf{B} ($\alpha > 0.01^\circ$), the shape of the IS spectrum is dominated by electron diffusion *along* the magnetic field lines. As collisions impede the motion of particles, electrons diffuse slower in a collisional plasma than in a collisionless one (where electrons move freely), which implies that the electrons stay closer to their original locations for longer periods of time. As a result, the correlation time of the signal scattered by the electrons also becomes longer, causing the broadening of the IS signal ACF and the associated narrowing of the signal spectrum in this aspect angle regime, as first explained by Sulzer & González (1999).

Spectrum dependence on electron density N_e and temperatures T_e and T_i has been studied by Milla & Kudeki (2011). Since at very small aspect angles the electron Gordeyev integral dominates the shape of the overall incoherent scatter spectrum, Milla & Kudeki (2011) found that in the limit of $\alpha \rightarrow 0^\circ$ the bandwidth of $\text{Re}\{J_e(\omega)\}$, and therefore the IS spectrum, varies according to

$$k^2 C_e^2 \frac{v_\perp}{v_\perp^2 + \Omega_e^2}. \quad (56)$$

Furthermore, using $v_\perp \approx v_{e/i} + v_{e/e}$ from the last section and taking $\Omega_e \gg v_\perp$, we can verify that the bandwidth dependence (56) is proportional to

$$\frac{N_e}{\sqrt{T_e}}. \quad (57)$$

However, as α increases, in a few hundredths of a degree, the dependance of the IS spectral width on N_e and T_e is exchanged, i.e., the bandwidth increases as either the density decreases or the temperature increases. The reason for this is the exchange of roles between particle diffusion in the directions across and along the magnetic field lines. It should be mentioned that collision effects become less significant at even larger aspect angles where the spectrum is shaped by ion dynamics. In that regime, the spectral shapes become independent of N_e as long as $kh_e \ll 1$.

The volumetric radar cross section (RCS) pertinent in ISR applications is given by (e.g., Farley, 1966; Milla & Kudeki, 2006)

$$\sigma_v \equiv 4\pi r_e^2 N_e \eta(\mathbf{k}) \quad (58)$$

where

$$\eta(\mathbf{k}) \equiv \int \frac{d\omega}{2\pi} \frac{\langle |n_e(\mathbf{k}, \omega)|^2 \rangle}{N_e}, \quad (59)$$

is an electron scattering efficiency factor (see Milla & Kudeki, 2006) and depends on the temperature ratio T_e/T_i and magnetic aspect angle α . A plot of this factor obtained from our collisional IS model is shown in Figure 11. As we can observe, if the plasma is in thermal equilibrium (i.e., if $T_e = T_i$), this factor is 1/2 at all angles α and compatible with (28). We can also see that $\eta(\mathbf{k})$ at $\alpha = 0^\circ$ increases in proportion to T_e/T_i . However, at large magnetic aspect angles, the efficiency factor shows a decrease with increasing T_e/T_i . In particular, note that our calculations for $\alpha = 90^\circ$ match the well-known formula $(1 + T_e/T_i)^{-1}$, as expected for moderate values of T_e/T_i and negligible Debye length (e.g., Farley, 1966). Note that for $\alpha \approx 1^\circ$ the factor is approximately independent of T_e/T_i , but otherwise it increases and decreases with the temperature ratio at small and large aspect angles, respectively.

9. Magnetoionic propagation effects on IS spectrum

A radiowave propagating through the ionosphere experiences changes in its polarization caused by the presence of the Earth's magnetic field. In this section, a model for incoherent scatter spectrum and cross-spectrum measurements that takes into account magnetoionic propagation effects is developed.

A mathematical description of radiowave propagation in an inhomogeneous magnetoplasma based on the Appleton-Hartree solution is presented. The resultant wave propagation model is used to formulate a soft-target radar equation in order to account for magnetoionic propagation effects on incoherent scatter spectrum and cross-spectrum models.

9.1 Propagation of electromagnetic waves in a homogeneous magnetoplasma

In the presence of an ambient magnetic field \mathbf{B}_0 , there are two possible and orthogonal modes of electromagnetic wave propagation in a plasma, and, therefore, any propagating field can be represented as the weighted superposition of these characteristic modes. Labeling the modes as ordinary (O) and extraordinary (X), the transverse component of an outgoing (transmitted) electric wave field, at a distance r from the origin, can be written in phasor form as

$$\mathbf{E}^t = A_O \left(\hat{\theta} - j\hat{\phi} \frac{F_O}{Y_L} \right) e^{-jk_0 n_O r} + A_X \left(\hat{\theta} - j\hat{\phi} \frac{F_X}{Y_L} \right) e^{-jk_0 n_X r}, \quad (60)$$

where A_O and A_X are the amplitudes of the O- and X-mode waves with refractive indices

$$n_{O/X}^2 = 1 - \frac{X}{1 - F_{O/X}} \quad (61)$$

specified by Appleton-Hartree equations (e.g., Budden, 1961), in which

$$F_{O/X} = \frac{Y_T^2 \mp \sqrt{Y_T^4 + 4Y_L^2(1-X)^2}}{2(1-X)}, \quad (62)$$

$$X \equiv \frac{\omega_p^2}{\omega^2}, \quad Y_L \equiv \frac{\Omega_e}{\omega} \cos \theta, \quad \text{and} \quad Y_T \equiv \frac{\Omega_e}{\omega} \sin \theta. \quad (63)$$

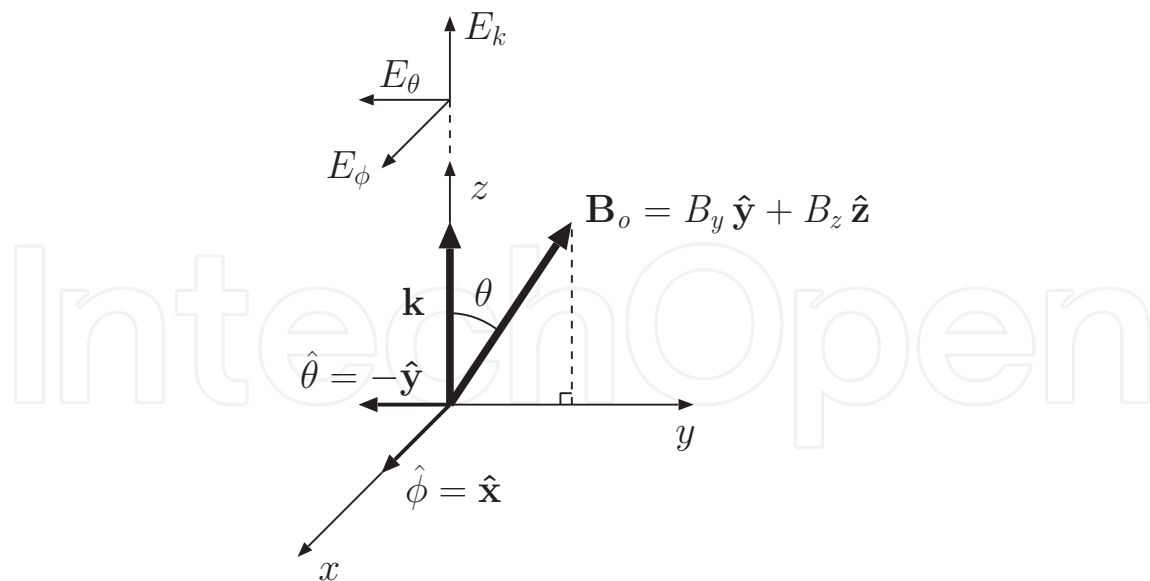


Fig. 12. Coordinate system used for analyzing wave propagation in a magnetized plasma. The magnetic field \mathbf{B}_o is on the yz -plane and angle θ is measured from \mathbf{B}_o to the propagation vector \mathbf{k} which is parallel to the $\hat{\mathbf{z}}$ -direction. The wave field \mathbf{E} has three mutually orthogonal components E_k , E_θ , and E_ϕ in directions $\hat{\mathbf{k}} = \hat{\mathbf{z}}$, $\hat{\boldsymbol{\theta}} = -\hat{\mathbf{y}}$, and $\hat{\boldsymbol{\phi}} = \hat{\mathbf{x}}$, respectively. $\hat{\boldsymbol{\theta}}$ is the direction of increasing θ and $\hat{\boldsymbol{\phi}} \equiv \hat{\mathbf{k}} \times \hat{\boldsymbol{\theta}}$.

Above $k_o = \omega/c$ is the free-space wavenumber, $\omega_p \equiv \sqrt{N_e e^2 / \epsilon_o m_e}$ and $\Omega_e = eB_o / m_e$ are the plasma- and electron gyro-frequencies, respectively, and θ is the angle measured from the magnetic field vector to the propagation direction $\hat{\mathbf{k}}$. Also, $\hat{\boldsymbol{\theta}}$ and $\hat{\boldsymbol{\phi}}$ are orthogonal unit vectors normal to $\hat{\mathbf{k}}$ as shown in Figure 12.

Note that $F_O F_X = -Y_L^2$ as demanded by the orthogonality of O- and X-mode terms in (60). Thus, $a \equiv \frac{F_O}{Y_L} = -\frac{Y_L}{F_X}$ denotes the axial ratio of elliptically polarized modes in (60), which in turn can be expressed in matrix notation as

$$\begin{bmatrix} E_\theta \\ E_\phi \end{bmatrix} = \begin{bmatrix} e^{-jk_o n_O r} & e^{-jk_o n_X r} \\ -jae^{-jk_o n_O r} & ja^{-1}e^{-jk_o n_X r} \end{bmatrix} \begin{bmatrix} A_O \\ A_X \end{bmatrix}, \quad (64)$$

where E_θ and E_ϕ are the transverse field components in $\hat{\boldsymbol{\theta}}$ and $\hat{\boldsymbol{\phi}}$ directions. Note that a can take values within the range $0 \leq |a| \leq 1$ and that the limits 0 and 1 correspond to the cases of linearly and circularly polarized propagation modes. Defining $\bar{n} \equiv \frac{n_O + n_X}{2}$ and $\Delta n \equiv \frac{n_O - n_X}{2}$, and considering $E_{\theta,o}$ and $E_{\phi,o}$ as the field components at the origin, the propagating electric field (64) can be recast as

$$\begin{bmatrix} E_\theta \\ E_\phi \end{bmatrix} = \frac{e^{-jk_o \bar{n} r}}{1 + a^2} \underbrace{\begin{bmatrix} e^{-jk_o \Delta n r} + a^2 e^{jk_o \Delta n r} & 2a \sin(k_o \Delta n r) \\ -2a \sin(k_o \Delta n r) & a^2 e^{-jk_o \Delta n r} + e^{jk_o \Delta n r} \end{bmatrix}}_{\bar{\mathbf{T}}} \begin{bmatrix} E_{\theta,o} \\ E_{\phi,o} \end{bmatrix}, \quad (65)$$

where $\bar{\mathbf{T}}$ is a propagator matrix that maps the fields at the origin into the fields at a distance r . Note that in the case of waves traveling in $-\hat{\mathbf{k}}$ direction, the same matrix $\bar{\mathbf{T}}$ can be used to propagate the fields from a distance r to the origin.

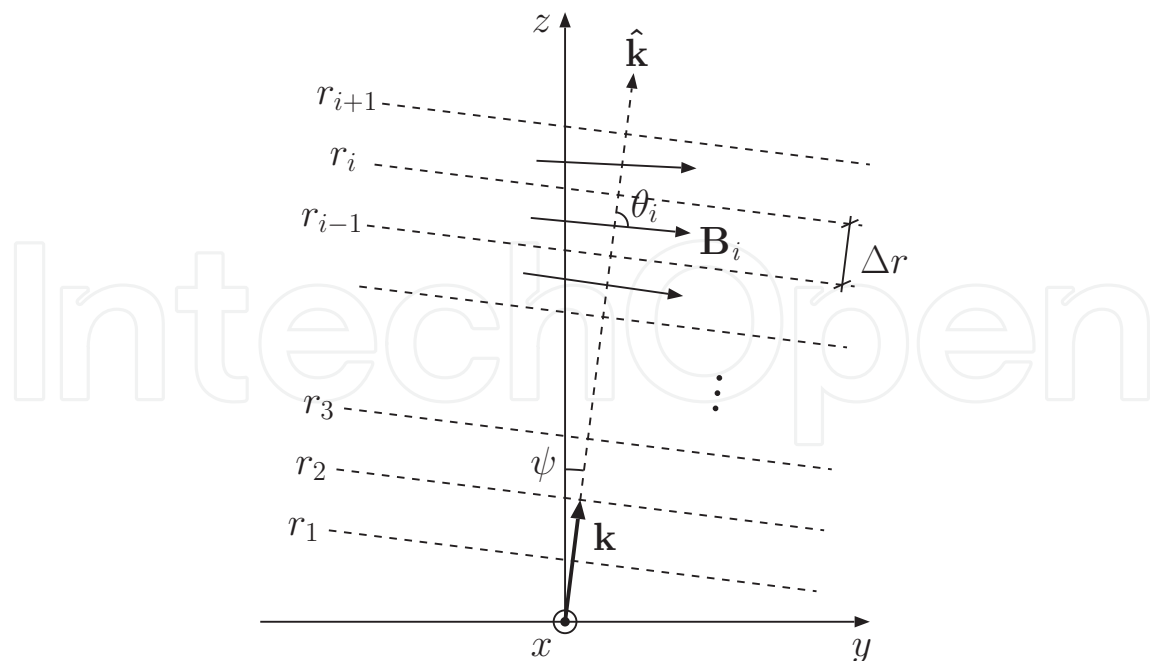


Fig. 13. Geometry of wave propagation in an inhomogeneous magnetized ionosphere.

Using the components of (65), we can re-express the outgoing electric field phasor $E_\theta \hat{\theta} + E_\phi \hat{\phi}$ as

$$\mathbf{E}^t = e^{-jk_o \bar{n}r} \left[e^{-jk_o \Delta nr} \hat{\mathbf{p}}_O \hat{\mathbf{p}}_O^H + e^{jk_o \Delta nr} \hat{\mathbf{p}}_X \hat{\mathbf{p}}_X^H \right] \mathbf{E}_o^t, \quad (66)$$

where \mathbf{E}_o^t is the wave field at the origin,

$$\hat{\mathbf{p}}_O = \frac{\hat{\theta} - ja \hat{\phi}}{\sqrt{1+a^2}} \quad \text{and} \quad \hat{\mathbf{p}}_X = \frac{-ja \hat{\theta} + \hat{\phi}}{\sqrt{1+a^2}} \quad (67)$$

are the orthonormal polarization vectors of the O- and X-mode waves, while $\hat{\mathbf{p}}_O^H$ and $\hat{\mathbf{p}}_X^H$ refer to their conjugate transpose counterparts.

9.2 Model for radiowave propagation in an inhomogeneous ionosphere

A radiowave propagating through an inhomogeneous magnetoplasma will experience refraction and polarization effects. At VHF frequencies, however, ionospheric refraction effects can be considered negligible for most propagation directions because the wave frequency ω exceeds the ionospheric plasma frequency ω_p by a wide margin (i.e., $X \ll 1$). But for the same set of frequencies, polarization changes are still significant despite the fact that the electron gyrofrequency Ω_e is much smaller than the wave frequency ω (i.e., $Y \ll 1$). The reason for this is that the distances traveled by the propagating fields are long enough (hundreds of kilometers) so that phase differences between wave components propagating in distinct modes accumulate to significant and detectable levels. Taking these elements into consideration and noting that, at VHF frequencies, the longitudinal components of the wave fields are negligibly small (as $X \ll 1$ and $Y \ll 1$), waves propagating through the ionosphere can be represented as TEM (transverse electromagnetic) waves.

Consider plane wave propagation in an inhomogeneous magnetized ionosphere in an arbitrary direction $\hat{\mathbf{k}}$. To model the electric field of the propagating wave, we can divide the

ionosphere in slabs of equal width (see Figure 13) perpendicular to the propagation direction such that within each slab the physical plasma parameters (as electron density, electron and ion temperatures, and magnetic field) can be considered constants.⁹ The transverse component of the wave electric field propagates from the bottom to the top of the i -th slab according to (66), that is

$$\mathbf{E}_i = e^{-jk_o\bar{n}_i\Delta r} \underbrace{\left[e^{-jk_o\Delta n_i\Delta r} \hat{\mathbf{p}}_O \hat{\mathbf{p}}_O^H + e^{jk_o\Delta n_i\Delta r} \hat{\mathbf{p}}_X \hat{\mathbf{p}}_X^H \right]}_{\bar{\mathbf{T}}_i} \mathbf{E}_{i-1}, \quad (68)$$

which is the superposition of the O- and X-modes of magnetoionic propagation detailed in the previous section. Above, $\bar{\mathbf{T}}_i$ denotes the i -th propagator matrix (expressed in cartesian coordinates), where $k_o \equiv 2\pi/\lambda_o$ is the free-space wavenumber, Δr is the width of the slab, and where $\bar{n}_i \equiv \frac{n_{O,i} + n_{X,i}}{2}$ and $\Delta n_i \equiv \frac{n_{O,i} - n_{X,i}}{2}$ are the mean and half difference between the refractive indices of the propagation modes in the i -th layer. The polarization vectors of the O- and X-modes are

$$\hat{\mathbf{p}}_O = \frac{\hat{\boldsymbol{\theta}} - ja_i \hat{\boldsymbol{\phi}}}{\sqrt{1 + a_i^2}} \quad \text{and} \quad \hat{\mathbf{p}}_X = \frac{-ja_i \hat{\boldsymbol{\theta}} + \hat{\boldsymbol{\phi}}}{\sqrt{1 + a_i^2}} \quad (69)$$

where $a_i \equiv \frac{F_{O,i}}{Y_{L,i}} = -\frac{Y_{L,i}}{F_{X,i}}$ is the polarization parameter, and $\hat{\boldsymbol{\theta}}_i$ and $\hat{\boldsymbol{\phi}}_i$ are a pair of mutually orthogonal unit vectors perpendicular to $\hat{\mathbf{k}}$ whose directions depend on the relative orientation of the propagation vector \mathbf{k} and the magnetic field \mathbf{B}_i (see Figure 12). Neglecting reflection from the interfaces between slabs, the field components of an upgoing plane wave propagating in the $+\hat{\mathbf{k}}$ direction (at a distance $r_i = i\Delta r$ from the origin) can be computed by the successive application of the propagator matrices; that is,

$$\mathbf{E}_i^u = \bar{\mathbf{T}}_i \cdots \bar{\mathbf{T}}_2 \bar{\mathbf{T}}_1 \mathbf{E}_o^u, \quad (70)$$

where \mathbf{E}_o^u is the wave field at the origin (perpendicular to $\hat{\mathbf{k}}$), and $\bar{\mathbf{T}}_1 \cdots \bar{\mathbf{T}}_i$ are the propagator matrices from the bottom layer to the i -th layer. Similarly, taking advantage of the bidirectionality of the propagator matrices, the field components of a downgoing plane wave propagating in the $-\hat{\mathbf{k}}$ direction (from the i -th layer to the ground) can be written as

$$\mathbf{E}_o^d = \bar{\mathbf{T}}_1 \bar{\mathbf{T}}_2 \cdots \bar{\mathbf{T}}_i \mathbf{E}_i^d, \quad (71)$$

where \mathbf{E}_i^d is the field at the top of the i -th layer.

In radar experiments, the transverse field component of the signal backscattered from a radar range $r_i = i\Delta r$ can be modeled as

$$\mathbf{E}_o^r \propto \kappa_i \underbrace{\bar{\mathbf{T}}_1 \bar{\mathbf{T}}_2 \cdots \bar{\mathbf{T}}_i \bar{\mathbf{T}}_i \cdots \bar{\mathbf{T}}_2 \bar{\mathbf{T}}_1}_{\bar{\mathbf{\Pi}}_i} \mathbf{E}_o^t, \quad (72)$$

where \mathbf{E}_o^t and \mathbf{E}_o^r are the fields transmitted and received by the radar antenna in the $\hat{\mathbf{k}}$ direction. Above, $\bar{\mathbf{\Pi}}_i$ denotes a two-way propagator matrix that accounts for the polarization effects on

⁹ In the ionosphere, electron density and plasma temperatures can be considered to be functions of altitude $f(z)$. Thus, the values of these physical parameters at any position \mathbf{r} from a radar placed at the origin are given by $f(r \cos \psi)$ where r is the radar range and ψ is the zenith angle.

the waves incident on and backscattered from the radar range r_i (upgoing and downgoing waves, respectively). In addition, κ_i is a random variable related to the radar cross section (RCS) of the scatterers at the range r_i (e.g., randomly moving ionospheric electrons).

We now consider an $\hat{\mathbf{x}}$ polarized radar antenna transmitting

$$\hat{\mathbf{p}}_1 = \frac{\hat{\mathbf{k}} \times \hat{\mathbf{k}} \times \hat{\mathbf{x}}}{|\hat{\mathbf{k}} \times \hat{\mathbf{k}} \times \hat{\mathbf{x}}|} \quad (73)$$

polarized waves field in $\hat{\mathbf{k}}$ direction. On reception, the same antenna would be co-polarized with incoming fields of identical polarization direction $\hat{\mathbf{p}}_1$. For an orthogonal $\hat{\mathbf{y}}$ polarized antenna

$$\hat{\mathbf{p}}_2 = \frac{\hat{\mathbf{k}} \times \hat{\mathbf{k}} \times \hat{\mathbf{y}}}{|\hat{\mathbf{k}} \times \hat{\mathbf{k}} \times \hat{\mathbf{y}}|} \quad (74)$$

would be the polarization direction of co-polarized fields. Let's assume that these two antennas, located at the geomagnetic equator, scan the ionosphere from north to south to construct power maps of the backscattered signals. In every pointing direction, narrow pulses are transmitted so that range filtering effects (due to the convolution of the pulse shape with the response of the ionosphere) can be ignored. In transmission, only the first antenna ($\hat{\mathbf{x}}$ polarized) is excited, while, in reception, both antennas are used to collect the backscattered signals. The two antennas then provide us with co- and cross-polarized output voltages

$$v_1(\hat{\mathbf{k}}) \propto \kappa_i \hat{\mathbf{p}}_1^T \bar{\mathbf{\Pi}}_i \hat{\mathbf{p}}_1 \quad \text{and} \quad v_2(\hat{\mathbf{k}}) \propto \kappa_i \hat{\mathbf{p}}_2^T \bar{\mathbf{\Pi}}_i \hat{\mathbf{p}}_1, \quad (75)$$

sampled at each range r_i , where the two-way propagator matrix $\bar{\mathbf{\Pi}}_i$ (defined above) is dependent on the electron density and magnetic field values along $\hat{\mathbf{k}}$ up to the radar range r_i . As κ_i is a random variable, the statistics of voltages (75) would be needed to characterize the scattering targets. For instance, the mean square values of v_1 and v_2 can be modeled as

$$\langle |v_1|^2 \rangle \propto \sigma_v \Gamma_1 \quad \text{and} \quad \langle |v_2|^2 \rangle \propto \sigma_v \Gamma_2, \quad (76)$$

where $\sigma_v = \langle |\kappa_i|^2 \rangle$ is the volumetric RCS of the medium, which is dependent on the electron density, temperature ratio, and magnetic aspect angle at any given range. In addition, Γ_1 and Γ_2 are polarization coefficients defined as

$$\Gamma_1 = \left| \hat{\mathbf{p}}_1^T \bar{\mathbf{\Pi}}_i \hat{\mathbf{p}}_1 \right|^2 \quad \text{and} \quad \Gamma_2 = \left| \hat{\mathbf{p}}_2^T \bar{\mathbf{\Pi}}_i \hat{\mathbf{p}}_1 \right|^2. \quad (77)$$

To simulate radar voltages using the model described above, an ionosphere with the electron density and T_e/T_i profiles displayed in Figure 14 was considered. In addition, the magnetic field was computed using the International Geomagnetic Reference Field (IGRF) model (e.g., Olsen et al., 2000). Finally, the simulations were performed for a 50 MHz radar at the location of the Jicamarca ISR in Peru and antenna polarizations $\hat{\mathbf{x}}$ and $\hat{\mathbf{y}}$ were taken to point in SE and NE directions as at Jicamarca.

Let us first analyze magnetoionic propagation effects on the simulated radar voltages, disregarding scattering effects. For this purpose, polarization coefficients Γ_1 and Γ_2 are displayed in Figure 15 as functions of distance and altitude from the radar (in the plots, the positive horizontal axis is directed north). Note that, at low altitudes, where there is

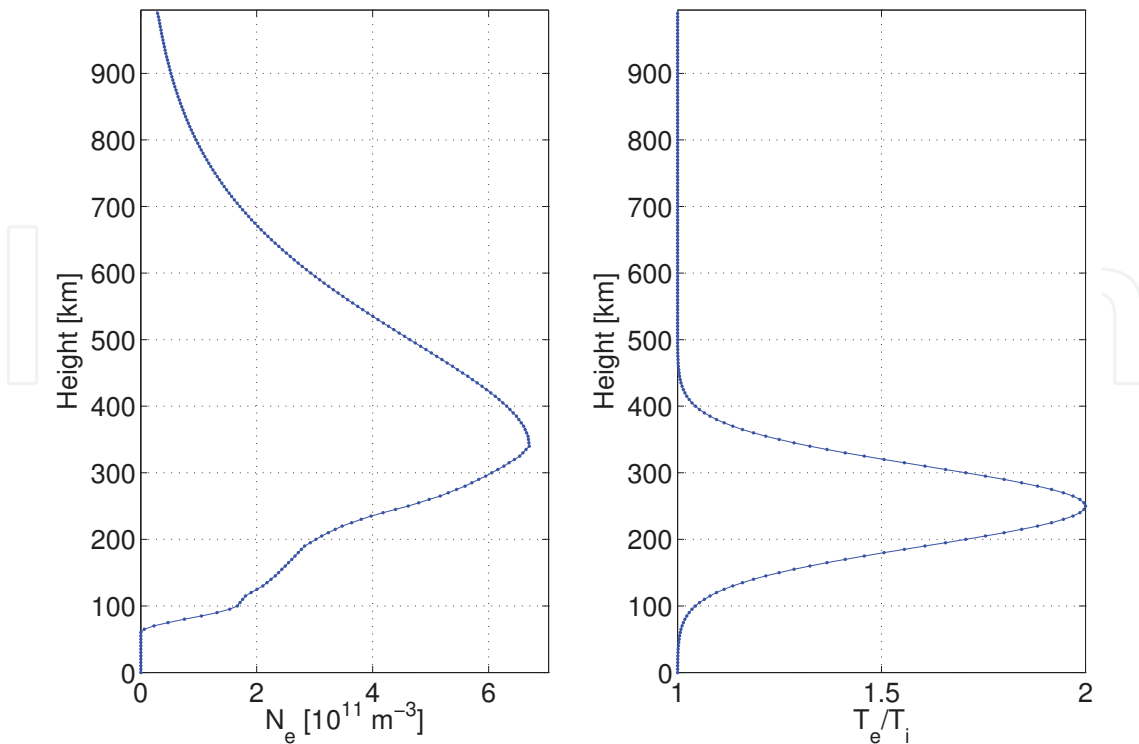


Fig. 14. Electron density and T_e/T_i profiles as functions of height.

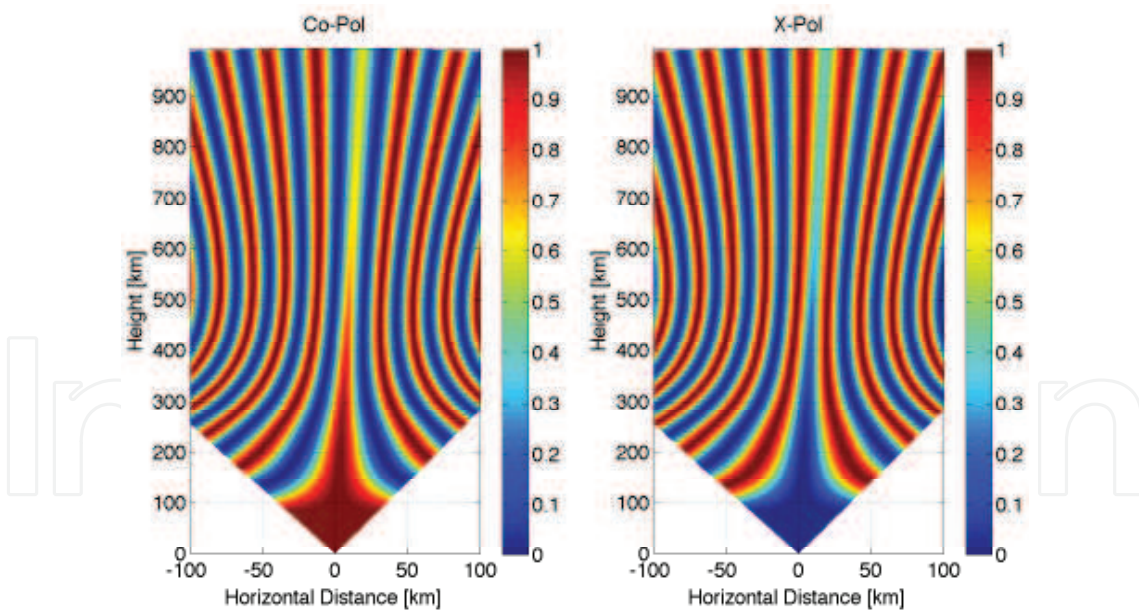


Fig. 15. Polarization coefficients for the mean square voltages detected by a pair of orthogonal linearly polarized antennas placed at Jicamarca. The antennas have very narrow beams and scan the ionosphere from north to south probing different magnetic aspect angle directions. Note that, for most pointing directions, the polarization of the detected fields rotates (Faraday rotation effect), except in the direction where the beam is pointed perpendicular to \mathbf{B} , in which case, the type of polarization changes from linear to circular (Cotton-Mouton effect).

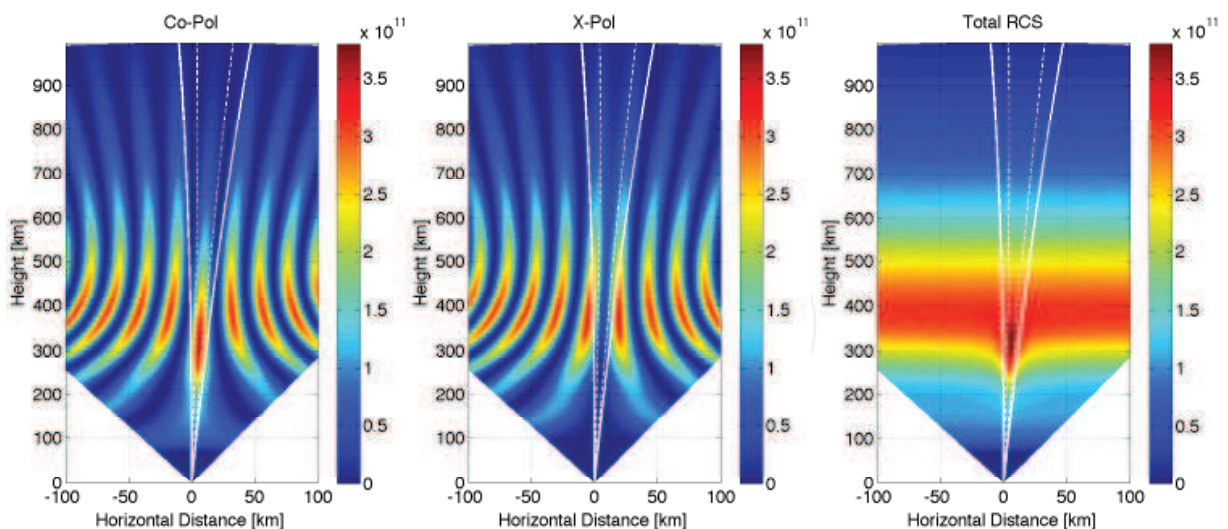


Fig. 16. Co-polarized (left panel), cross-polarized (middle panel), and total (right panel) backscattered power detected by a pair of orthogonal linearly polarized antennas (see caption of Figure 15). Power levels are displayed in units of electron density. In each plot, the dashed white lines indicate the directions half a degree away from perpendicular to \mathbf{B} , while the continuous lines correspond to the directions one degree off.

no ionosphere, signal returns will be detected only by the co-polarized antenna (i.e., by the same antenna used on transmission). However, as the signal propagates farther through the ionosphere, magnetoionic effects start taking place. We can appreciate that, for most of the propagation directions, the polarization vector of the detected field rotates such that signal from one polarization goes to the other as the radar range increases (Faraday rotation effect). Note, however, that there is a direction in which the wave polarization does not rotate much. In this direction, the antenna beams are pointed perpendicular to the Earth's magnetic field, and it can be observed that the polarization of the detected fields varies progressively from linear to circular as a function of height (Cotton–Mouton effect). Finally, note that at higher altitudes, where the ionosphere vanishes, no more magnetoionic effects take place, and the polarization of the detected signal approaches a final state.

Next, scattering and propagation effects are considered in the simulation of the backscattered power collected by the pair of orthogonal antennas described above. The incoherent scatter volumetric RCS formulated in the previous section is used in the calculations. In Figure 16, the simulated co-polarized (left panel) and cross-polarized (middle panel) power data are displayed as functions of distance and altitude from the radar. In addition, the right panel depicts the total power detected by both antennas. Note that power levels are displayed as volumetric radar cross sections divided by $4\pi r_e^2$ (i.e., power levels are in units of electron density). In each plot, the dashed white lines indicate the directions half a degree away from perpendicular to \mathbf{B} , while the continuous lines correspond to the directions one degree off.

In the plots, we can observe that there is negligible backscattered power at low altitudes. At higher altitudes between approximately 200 and 700 km (where polarization effects are significant), co- and cross-polarized power maps exhibit features that are similar to the ones observed in Figure 15. Note, however, that there is an enhancement of the detected power in the direction where the antenna beams are pointed perpendicular to \mathbf{B} ; this can be observed more clearly in the plot of the total power (right panel of Figure 16). This feature

is characteristic of the incoherent scatter process for probing directions perpendicular to \mathbf{B} and for heights where electron temperature exceeds the ion temperature (i.e., $T_e > T_i$) as described before. At even higher altitudes, scattered signals become weaker and weaker as the ionospheric electron density vanishes.

To model incoherent scatter radar measurements using the propagation model presented in this section, an extra level of complexity has to be considered because, within the range of aspect angles illuminated by the antenna beams, propagation and scattering effects vary quite rapidly. For this reason, the measured backscattered radar signals need to be carefully modeled taking into account the shapes of the antenna beams. A model for the beam-weighted incoherent scatter spectrum that considers magnetoionic propagation and collisional effects is formulated next.

9.3 Soft-target radar equation and magnetoionic propagation

In this section, the soft-target radar equation is reformulated using the wave propagation model described above. Consider a radar system composed of a set of antenna arrays (located in the same area) with matched filter receivers connected to the antennas used in reception. The mean square voltage at the output of the i -th receiver can be expressed as

$$\langle |v_i(t)|^2 \rangle = E_t K_i \int dr d\Omega \frac{d\omega}{2\pi} \frac{|\mathcal{T}(\hat{\mathbf{r}})|^2 |\mathcal{R}_i(\hat{\mathbf{r}})|^2}{k^2} \Gamma_i(\mathbf{r}) \frac{|\chi(t - \frac{2r}{c}, \omega)|^2}{4\pi r^2} \sigma_v(\mathbf{k}, \omega), \quad (78)$$

where t is the radar delay, E_t is the total energy of the transmitted radar pulse, and K_i is the i -th calibration constant (a proportionality factor that accounts for the gains and losses along the i -th signal path). Integrals are taken over range r , solid angle Ω , and Doppler frequency $\omega/2\pi$. In addition, $\mathbf{k} = -2k_o \hat{\mathbf{r}}$ denotes the relevant Bragg vector for a radar with a carrier wavenumber k_o and associated wavelength λ . Above, $\mathcal{T}(\hat{\mathbf{r}})$ and $\mathcal{R}_i(\hat{\mathbf{r}})$ are the antenna factors of the arrays used in transmission and reception. Note that $|\mathcal{T}(\hat{\mathbf{r}})|^2$ and $|\mathcal{R}_i(\hat{\mathbf{r}})|^2$ are antenna gain patterns and the product $|\mathcal{T}(\hat{\mathbf{r}})|^2 |\mathcal{R}_i(\hat{\mathbf{r}})|^2$ is the corresponding two-way radiation pattern. The polarization coefficient $\Gamma_i(\mathbf{r})$ is defined as

$$\Gamma_i(\mathbf{r}) = \left| \hat{\mathbf{p}}_i^T \bar{\mathbf{\Pi}}(\mathbf{r}) \hat{\mathbf{p}}_t \right|^2, \quad (79)$$

where $\hat{\mathbf{p}}_t$ and $\hat{\mathbf{p}}_i$ are the polarization unit vectors of the transmitting and receiving antennas, and $\bar{\mathbf{\Pi}}(\mathbf{r})$ is the two-way propagator matrix for the wave field components propagating along $\hat{\mathbf{r}}$ (incident on and backscattered from the range r). Note that $\hat{\mathbf{p}}_t$ and $\hat{\mathbf{p}}_i$ are normal to $\hat{\mathbf{r}}$ because propagating fields are represented as TEM waves. In addition, $\chi(t, \omega)$ is the radar ambiguity function and $\sigma_v(\mathbf{k}, \omega)$ is the volumetric RCS spectrum, functions that have been defined before. Similarly, the cross-correlation of the voltages at the outputs of the i -th and j -th receivers can be expressed as

$$\langle v_i(t) v_j^*(t) \rangle = E_t K_{i,j} \int dr d\Omega \frac{d\omega}{2\pi} \frac{|\mathcal{T}(\hat{\mathbf{r}})|^2 \mathcal{R}_i(\hat{\mathbf{r}}) \mathcal{R}_j^*(\hat{\mathbf{r}})}{k^2} \Gamma_{i,j}(\mathbf{r}) \frac{|\chi(t - \frac{2r}{c}, \omega)|^2}{4\pi r^2} \sigma_v(\mathbf{k}, \omega), \quad (80)$$

where $K_{i,j}$ is a cross-calibration constant (dependent on gains and losses along the i -th and j -th signal paths), and $\Gamma_{i,j}(\mathbf{r})$ is a cross-polarization coefficient defined as

$$\Gamma_{i,j}(\mathbf{r}) = \left(\hat{\mathbf{p}}_i^T \bar{\mathbf{\Pi}}(\mathbf{r}) \hat{\mathbf{p}}_t \right) \left(\hat{\mathbf{p}}_j^T \bar{\mathbf{\Pi}}(\mathbf{r}) \hat{\mathbf{p}}_t \right)^*. \quad (81)$$

Note that dispersion of the pulse shape due to wave propagation effects has been neglected in our model.

Denoting by $S_i(\omega)$ the self-spectrum of the signal at the output of the i -th receiver and applying Parseval's theorem, we have that

$$\langle |v_i(t)|^2 \rangle = \int \frac{d\omega}{2\pi} S_i(\omega). \quad (82)$$

Likewise, the cross-spectrum $S_{i,j}(\omega)$ and the cross-correlation of the signals at the outputs of the i -th and j -th receivers are related by

$$\langle v_i(t)v_j^*(t) \rangle = \int \frac{d\omega}{2\pi} S_{i,j}(\omega). \quad (83)$$

Assuming that the ambiguity function is almost flat within the bandwidth of the RCS spectrum $\sigma_v(\mathbf{k}, \omega)$ (which is a valid approximation in the case of short-pulse radar applications), we can use equations (78) and (80) to obtain the following beam-weighted spectrum and cross-spectrum models:

$$S_i(\omega) = E_t K_i \int dr \frac{|\chi(t - \frac{2r}{c})|^2}{4\pi r^2} \int d\Omega \frac{|\mathcal{T}(\hat{\mathbf{r}})|^2 |\mathcal{R}_i(\hat{\mathbf{r}})|^2}{k^2} \Gamma_i(\mathbf{r}) \sigma_v(\mathbf{k}, \omega) \quad (84)$$

and

$$S_{i,j}(\omega) = E_t K_{i,j} \int dr \frac{|\chi(t - \frac{2r}{c})|^2}{4\pi r^2} \int d\Omega \frac{|\mathcal{T}(\hat{\mathbf{r}})|^2 \mathcal{R}_i(\hat{\mathbf{r}}) \mathcal{R}_j^*(\hat{\mathbf{r}})}{k^2} \Gamma_{i,j}(\mathbf{r}) \sigma_v(\mathbf{k}, \omega), \quad (85)$$

where

$$\chi(t) = \frac{1}{T} f^*(-t) * f(t) \quad (86)$$

is the normalized auto-correlation of the pulse waveform $f(t)$. In the radar equations (84) and (85), the polarization coefficients $\Gamma_i(\mathbf{r})$ and $\Gamma_{i,j}(\mathbf{r})$ effectively modify the radiation patterns; thus, the spectrum shapes are dependent not only on the scattering process but also on the modes of propagation. This dependence further complicates the spectrum analysis of radar data and the inversion of physical parameters.

10. Summary

In this chapter we have described the operation of ionospheric incoherent scatter radars (ISR) and the signal spectrum models underlying the operation of such radars. ISR's are the premier remote sensing instruments used to study the ionosphere and Earth's upper atmosphere. First generation operational ISR's were built in the early 1960's — e.g., Jicamarca in Peru and Arecibo in Puerto Rico — and ISR's continue to play a crucial role in our studies of Earth's near space environment. These instruments are primarily used to monitor the electron densities and drifts, as well as temperatures and chemical composition of ionospheric plasmas. The latest generation of ISR's include the AMISR — advanced modular ISR — series which are planned to be deployed around the globe and then re-located depending on emerging science needs. With increasing ISR units around the globe, there will be a larger demand on radar engineers and technicians familiar with ISR modes and the underlying scattering theory. For that reason, in our presentation in this chapter, as well as in our recent papers (Kudeki & Milla, 2011; Milla & Kudeki, 2011), we have taken an "engineering approach" to describe the theory of the incoherent scatter spectrum. Complementary physics based descriptions of the same processes can be found in many of the original ISR papers included in references.

11. Acknowledgements

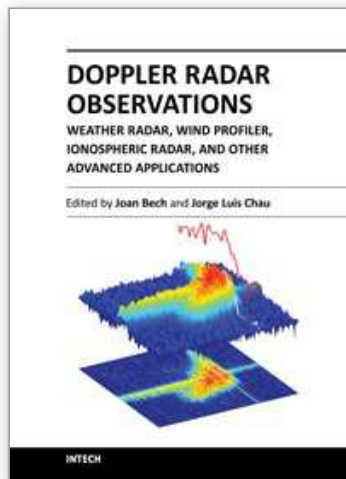
This chapter is based upon work supported by the National Science Foundation under Grant No. 0215246 and 1027161.

12. References

- Bowles, K. L. (1958). Observation of vertical-incidence scatter from the ionosphere at 41 mc/sec, *Physical Review Letters* 1(12): 454–455.
- Budden, K. G. (1961). *Radio Waves in the Ionosphere*, Cambridge University Press, Cambridge, United Kingdom.
- Callen, H. B. & Welton, T. A. (1951). Irreversibility and generalized noise, *Physical Review* 83(1): 34–40.
- Callen, J. D. (2006). *Fundamentals of Plasma Physics*, Chapter 2 – Coulomb Collisions.
URL: <http://homepages.cae.wisc.edu/callen/book.html>
- Chandrasekhar, S. (1942). *Principles of Stellar Dynamics*, University of Chicago Press, Chicago.
- Chandrasekhar, S. (1943). Stochastic problems in physics and astronomy, *Reviews of Modern Physics* 15(1): 1–89.
- Chau, J. L. & Kudeki, E. (2006). First E- and D-region incoherent scatter spectra observed over Jicamarca, *Annales Geophysicae* 24(5): 1295–1303.
- Dougherty, J. P. (1964). Model Fokker-Planck equation for a plasma and its solution, *The Physics of Fluids* 7(11): 1788–1799.
- Dougherty, J. P. & Farley, D. T. (1963). A theory of incoherent scattering of radio waves by a plasma 3. Scattering in a partly ionized gas, *Journal of Geophysical Research* 68: 5473–5486.
- Farley, D. T. (1964). The effect of Coulomb collisions on incoherent scattering of radio waves by a plasma, *Journal of Geophysical Research* 69(1): 197–200.
- Farley, D. T. (1966). A theory of incoherent scattering of radio waves by a plasma 4. The effect of unequal ion and electron temperatures, *Journal of Geophysical Research* 71(17): 4091–4098.
- Gillespie, D. T. (1996a). The mathematics of Brownian motion and Johnson noise, *American Journal of Physics* 64(3): 225–240.
- Gillespie, D. T. (1996b). The multivariate Langevin and Fokker–Planck equations, *American Journal of Physics* 64(10): 1246–1257.
- Gordon, W. E. (1958). Incoherent scattering of radio waves by free electrons with applications to space exploration by radar, *Proceedings of the IRE* 46(11): 1824–1829.
- Hagfors, T. & Brockelman, R. A. (1971). A theory of collision dominated electron density fluctuations in a plasma with applications to incoherent scattering, *The Physics of Fluids* 14(6): 1143–1151.
- Holod, I., Zagorodny, A. & Weiland, J. (2005). Anisotropic diffusion across an external magnetic field and large-scale fluctuations in magnetized plasmas, *Physical Review E* 71(4): 1–11.
- Kudeki, E., Bhattacharyya, S. & Woodman, R. F. (1999). A new approach in incoherent scatter F region $E \times B$ drift measurements at Jicamarca, *Journal of Geophysical Research* 104(A12): 28145–28162.
- Kudeki, E. & Milla, M. A. (2011). Incoherent scatter spectral theories—Part I: A general framework and results for small magnetic aspect angles, *IEEE Transactions on Geoscience and Remote Sensing* 49(1): 315–328.

- Mathews, J. D. (1984). The incoherent scatter radar as a tool for studying the ionospheric D-region, *Journal of Atmospheric and Terrestrial Physics* 46(32): 975–986.
- Milla, M. A. & Kudeki, E. (2006). F-region electron density and T_e/T_i measurements using incoherent scatter power data collected at ALTAIR, *Annales Geophysicae* 24(5): 1333–1342.
- Milla, M. A. & Kudeki, E. (2009). Particle dynamics description of “BGK collisions” as a Poisson process, *Journal of Geophysical Research* 114(7): 1–4.
- Milla, M. A. & Kudeki, E. (2011). Incoherent scatter spectral theories–Part II: Modeling the spectrum for modes propagating perpendicular to \mathbf{B} , *IEEE Transactions on Geoscience and Remote Sensing* 49(1): 329–345.
- Olsen, N., Sabaka, T. J. & Tøffner-Clausen, L. (2000). Determination of the IGRF 2000 model, *Earth, Planets and Space* 52(12): 1175–1182.
- Rosenbluth, M. N., MacDonald, W. M. & Judd, D. L. (1957). Fokker-Planck equation for an inverse-square force, *Physical Review* 107(1): 1–6.
- Sulzer, M. P. & González, S. A. (1999). The effect of electron Coulomb collisions on the incoherent scatter spectrum in the F region at Jicamarca, *Journal of Geophysical Research* 104(A10): 22535–22551.
- Uhlenbeck, G. E. & Ornstein, L. S. (1930). On the theory of the Brownian motion, *Physical Review* 36(5): 823–841.
- Woodman, R. F. (1967). *Incoherent scattering of electromagnetic waves by a plasma*, PhD thesis, Harvard University, Cambridge, Massachusetts.
- Yeh, K. C. & Liu, C. H. (1972). *Theory of Ionospheric Waves*, Vol. 17 of *International Geophysics*, Elsevier.

IntechOpen



Doppler Radar Observations - Weather Radar, Wind Profiler, Ionospheric Radar, and Other Advanced Applications

Edited by Dr. Joan Bech

ISBN 978-953-51-0496-4

Hard cover, 470 pages

Publisher InTech

Published online 05, April, 2012

Published in print edition April, 2012

Doppler radar systems have been instrumental to improve our understanding and monitoring capabilities of phenomena taking place in the low, middle, and upper atmosphere. Weather radars, wind profilers, and incoherent and coherent scatter radars implementing Doppler techniques are now used routinely both in research and operational applications by scientists and practitioners. This book brings together a collection of eighteen essays by international leading authors devoted to different applications of ground based Doppler radars. Topics covered include, among others, severe weather surveillance, precipitation estimation and nowcasting, wind and turbulence retrievals, ionospheric radar and volcanological applications of Doppler radar. The book is ideally suited for graduate students looking for an introduction to the field or professionals intending to refresh or update their knowledge on Doppler radar applications.

How to reference

In order to correctly reference this scholarly work, feel free to copy and paste the following:

Erhan Kudeki and Marco Milla (2012). Incoherent Scatter Radar - Spectral Signal Model and Ionospheric Applications, Doppler Radar Observations - Weather Radar, Wind Profiler, Ionospheric Radar, and Other Advanced Applications, Dr. Joan Bech (Ed.), ISBN: 978-953-51-0496-4, InTech, Available from: <http://www.intechopen.com/books/doppler-radar-observations-weather-radar-wind-profiler-ionospheric-radar-and-other-advanced-applications/incoherent-scatter-radar-spectral-measurements-and-ionospheric-applications>

INTECH
open science | open minds

InTech Europe

University Campus STeP Ri
Slavka Krautzeka 83/A
51000 Rijeka, Croatia
Phone: +385 (51) 770 447
Fax: +385 (51) 686 166
www.intechopen.com

InTech China

Unit 405, Office Block, Hotel Equatorial Shanghai
No.65, Yan An Road (West), Shanghai, 200040, China
中国上海市延安西路65号上海国际贵都大饭店办公楼405单元
Phone: +86-21-62489820
Fax: +86-21-62489821

© 2012 The Author(s). Licensee IntechOpen. This is an open access article distributed under the terms of the [Creative Commons Attribution 3.0 License](#), which permits unrestricted use, distribution, and reproduction in any medium, provided the original work is properly cited.

IntechOpen

IntechOpen